

Ferroelectricity in molecular solids: a review of electrodynamic properties

This content has been downloaded from IOPscience. Please scroll down to see the full text.

2015 Rep. Prog. Phys. 78 096501

(<http://iopscience.iop.org/0034-4885/78/9/096501>)

View [the table of contents for this issue](#), or go to the [journal homepage](#) for more

Download details:

IP Address: 141.58.18.202

This content was downloaded on 27/07/2015 at 21:19

Please note that [terms and conditions apply](#).

Review Article

Ferroelectricity in molecular solids: a review of electrodynamic properties

S Tomić¹ and M Dressel²¹ Institut za fiziku, PO Box 304, HR-10001 Zagreb, Croatia² 1. Physikalisches Institut, Universität Stuttgart, Pfaffenwaldring 57, D-70550 Stuttgart, GermanyE-mail: stomic@ifs.hr and dressel@pi1.physik.uni-stuttgart.de

Received 24 April 2015

Accepted for publication 18 May 2015

Published 27 July 2015



Invited by Laura Greene

Abstract

In conventional ferroelectrics the polarization is induced either by the relative displacement of positive and negative ions due to a lattice distortion or by the collective alignment of permanent electric dipoles. Strongly correlated materials with the inversion-symmetry-broken ground states feature electronic ferroelectricity, a phenomenon which has recently caught the attention of condensed matter physicists due to its great fundamental and technological importance. The discovery of electronic ferroelectricity in one and two-dimensional molecular solids is an exciting development because they show a rich variety of nonlinear properties and complex electrodynamic, including nontrivial emergent excitations. We summarize key experimental results, sketch the current theoretical understanding and outline promising prospects of this phenomenon which have great potential for future electronic devices.

Keywords: ferroelectricity, molecular solids, strongly correlated electrons, optical properties, dielectric properties

(Some figures may appear in colour only in the online journal)

1. Introduction

Strongly correlated electrons may undergo various types of collective condensations yielding novel and unexpected states in solids with diverse macroscopic properties [1–4]. The fine interplay of charge, spin, lattice and orbital interactions leads to numerable broken-symmetry electronic ground states and novel quantum phenomena, such as high-temperature superconductivity, colossal magnetoresistance, charge and spin orders, electronic ferroelectricity, multiferroicity, quantum Hall effect and spin liquids. These states are fundamental to the understanding of some of the most useful and intriguing properties of technologically advanced materials. For instance, layered cuprates, organic superconductors and manganites are famous for unconventional superconductivity and very large magnetoresistance effect; the two physical properties that are nowadays widely used in medicine,

high-tech electronic and data storage devices. Among them, charge-ordered phases, in particular those with electronic ferroelectricity hold a prominent place due to a rich variety of nonlinear properties and complex dynamics, including collective excitations [5–8].

Electronic or charge-driven ferroelectricity is a novel class of ferroelectricity in which electronic charge degrees of freedom with electron–electron interactions give rise to a macroscopic electric polarization and a charge-order phase transition. Signatures of this kind of ferroelectricity has been found in transition-metal compounds and low-dimensional charge-transfer molecular solids. Theoretically, electronic ferroelectricity was first shown to arise in the insulating phase of the Falicov–Kimball model [9]. This system possesses strong correlations between itinerant and localized electrons resulting in the charge density which breaks the inversion symmetry of the crystal lattice and establish electronic ferroelectricity.

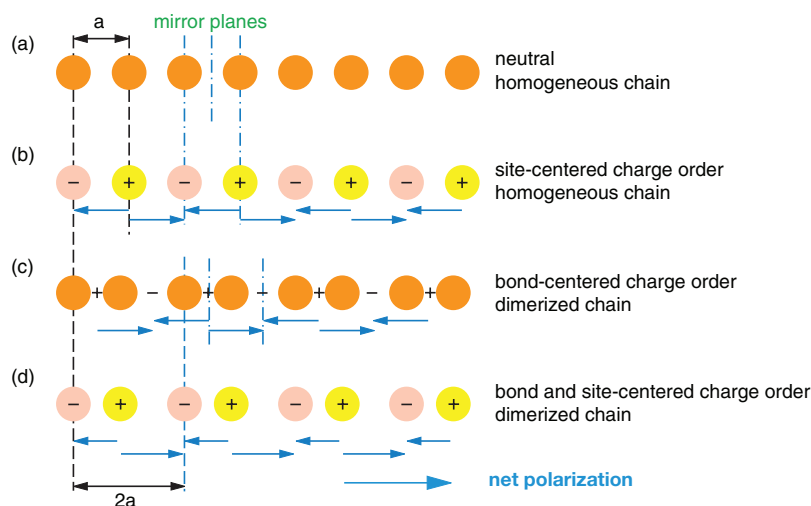


Figure 1. Schematic explanation of the basic mechanism by which charge ordering gives rise to electronic ferroelectricity (following [11]). Charge order breaks the inversion symmetry between the sites, but only together with a lattice dimerization, inversion symmetry is completely lost and a net polarization remains.

Recently, the basic mechanism by which the charge ordering can lead to ferroelectricity was worked out by Efremov *et al* [10]. As depicted in figure 1, the concomitant presence of non-equivalent sites and bonds breaks the inversion symmetry yielding a net dipole moment so that ferroelectricity can be developed at long ranges [11]. Non-equivalent sites and bonds are not necessarily associated with site-centered and bond-centered charge ordering; rather they may be simply due to the presence of charge sites with different valencies and to native crystallographic structure, respectively.

Different processes may be involved in the charge ordering phase transition establishing ferroelectric ground state so that each system needs to be studied separately. Random potential due to internal heterogeneity may also cause profound effects on the material electronic properties and the formation of the charge ordering. It sometimes enhances the competition between phases and consequently suppresses the ordering at longer scale resulting in relaxor ferroelectricity and glassy behavior [12, 13]. For such a domain-like ferroelectricity, the loss of inversion symmetry happens only at a local scale, while the symmetry of the overall crystal can be preserved [14]. Finally, a most recent worldwide attention is focused on materials with magneto-electric coupling in which ferroelectricity and magnetism coexist, widely known as multiferroics. Several extensive reviews were recently dedicated to this subject [11, 15, 16].

Although signatures of electronic ferroelectricity such as large dielectric constant, characteristic dielectric dispersion, hysteresis in polarization, second-harmonic generation, ultrafast dynamics, switching, bistable resistance and domain-wall dynamics have been observed in low-dimensional organic solids, a complete evidence as in conventional ferroelectrics and full understanding in most cases is still missing. Among others, open issues concern the nature of collective charge excitations in the charge-driven ferroelectric phases as well as their coupling to applied dc and ac fields. And while some of their features such as screened Arrhenius-like dispersion resemble the well-established electrostatics of

conventional charge-density waves (CDW) in one-dimension [17], others like giant nonlinear conductivity and negative differential resistance appear to be quite different and have not been encountered until now. Distinct mechanisms have been suggested to explain these remarkable effects, ranging from melting of charge order to dielectric breakdown and sliding. Equally, confronting views have been advanced concerning the mechanism behind charge-order phase transition and associated ferroelectricity ranging from purely Coulomb-driven to cation-anion hydrogen bonding interactions. Recently magneto-dielectric effects been proposed in several layered organics showing relaxor ferroelectricity, and possible multiferroicity involving coupled order-disorder ferroelectricity and magnetic order. Several theories have been put forward to explain these findings indicating the presence of quantum electric dipoles due to frustration and an important role of spin-charge coupling in the formation of the low-temperature phase in the charge and spin sectors.

Evidently, a quest for organic ferroelectricity has been a rapidly evolving field with many important results discovered during the last decade [18, 19]. An extensive review published in 2008 is dedicated to the development of novel routes for design of organic ferroelectrics with a critical eye on the possible areas of future applications [20]. Another excellent but specialized book chapter published in the same year covers theoretical models of electronic ferroelectricity due to charge ordering in one-dimensional organic charge-transfer compounds based on TMTTF molecules [21]; some experimental aspects of one-dimensional ferroelectric systems can be found in Monceau's review [22]. Two papers from 2006 provide an overview of relaxor ferroelectricity associated with the neutral-ionic valence instability [23, 24]. With these exceptions no similar attempt was undertaken until now.

The present paper is meant to give a survey of recent achievements in the studies of electrostatics of layered molecular charge-transfer solids based on BEDT-TTF molecule in search for electronic ferroelectricity. Besides the comprehensive presentation of the relevant findings, for sake

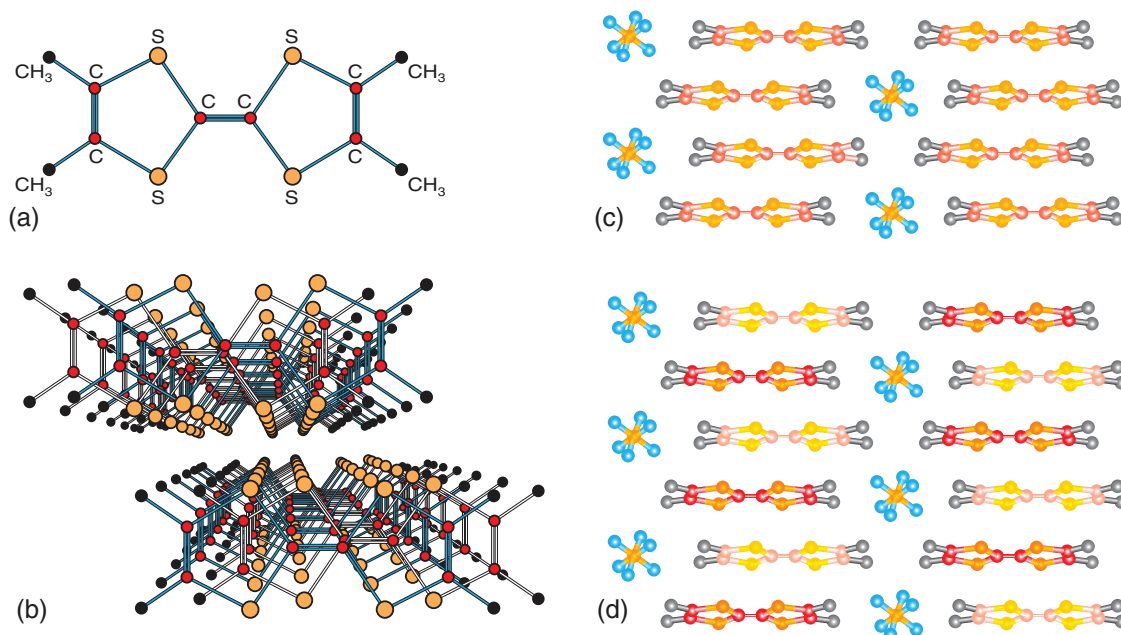


Figure 2. (a) Schematic drawing of a TMTTF molecule. (b) The nearly planar tetramethyltetrafulvalene (TMTTF) cations stack in columns extending along the a -axis and form layers in the (ab) -plane. (c) Side view of the extended unit cell of $(\text{TMTTF})_2\text{AsF}_6$: The triclinic unit cell (space group $\overline{P}1$) consists of two dimerized TMTTF molecules and one monovalent anion $X = \text{AsF}_6^-$. The anions X separate these stacks along the c -direction. (d) In the case of charge order the molecules on the dimer carry unequal charge, as indicated by the different color density. The unit cell does not double.

of comparison we include the state of the art for the one-dimensional systems based on TMTTF and TTF molecules. With this goal in mind and for the convenience of readers this review is arranged by particular classes of materials according to their dimensionality and basic molecular units. We begin with the ferroelectricity in $(\text{TMTTF})_2X$ and TTF-CA whose properties are understood rather well after significant progress made in the last decade. We then turn to weakly dimerized frustrated two-dimensional systems with BEDT-TTF molecules forming anisotropic triangular lattice. Within each section, ferroelectric phase transition physics including structural aspects and charge-sensitive features is followed by the presentation of collective effects and excitations through dielectric and optical properties, nonlinear response and time-dependent phenomena with current theoretical approaches discussed where appropriate. In the last part of this review we discuss the experimental situation and its challenges in the strongly-dimerized frustrated two-dimensional BEDT-TTF systems where improved experimental probes and complementary advances in theoretical approaches are required to provide very much needed relevant new insights into the questions related to origin of ferroelectric-like dielectric dispersion. We conclude by pointing out essential aspects of electronic ferroelectricity phenomena in molecular solids, spelling out unresolved issues and indicating future perspectives.

2. Charge order in one-dimensional $(\text{TMTTF})_2X$

The one-dimensional organic conductors $(\text{TMTTF})_2X$ are dimerized Mott insulators with one hole per TMTTF dimer at high temperatures. TMTTF stands for tetramethyltetrafulvalene with centrosymmetric anions X such as

PF_6^- , AsF_6^- , SbF_6^- , Br^- and noncentrosymmetric anions such as ReO_4^- , ClO_4^- , BF_4^- (figure 2). Depending on the nature of the anions a charge-ordered (CO) state develops at low temperatures, in which the TMTTF molecules become non-equivalent within the dimer (the case shown in figures 1(d) and 2(d)). The CO phase transition (T_{CO}) and the low-temperature state bears some fingerprints characteristic for ferroelectricity including structural changes and charge disproportionation due to symmetry breaking, and characteristic dielectric response.

2.1. Ferroelectric phase transition due to charge ordering

Charge disproportionation $2\delta_p$ has been established by nuclear magnetic resonance (NMR) [25–27] and infrared vibrational spectroscopy measurements [28, 29] showing a $4k_{\text{F}}$ pattern; within the unit cell the two TMTTF molecules carry $0.63e$ and $0.37e$, respectively. The temperature-dependent order parameter can be traced by following the NMR spectral lines of two ^{13}C nuclei with inequivalent hyperfine coupling belonging to the central C=C sites of the TMTTF molecules. The formation of two different, charge-rich and charge-poor, molecular environments is reflected in the splitting of each line with no associated magnetic anomalies; it steadily increases with decreasing temperature in the way characteristic of the second-order phase transition within mean-field theory (figure 3).

Equally, the order parameter can be extracted from the charge-sensitive stretching modes $\nu_3(A_g)$ and $\nu_{28}(b_{1u})$ of the central and outer C=C double bonds of TMTTF molecule. The position in frequency splits upon passing through the CO transition as demonstrated in figures 4(a)–(c). It is noteworthy that the $\nu_3(A_{1u})$ mode is totally symmetric and thus only Raman-active; however, it becomes infrared active for light polarized

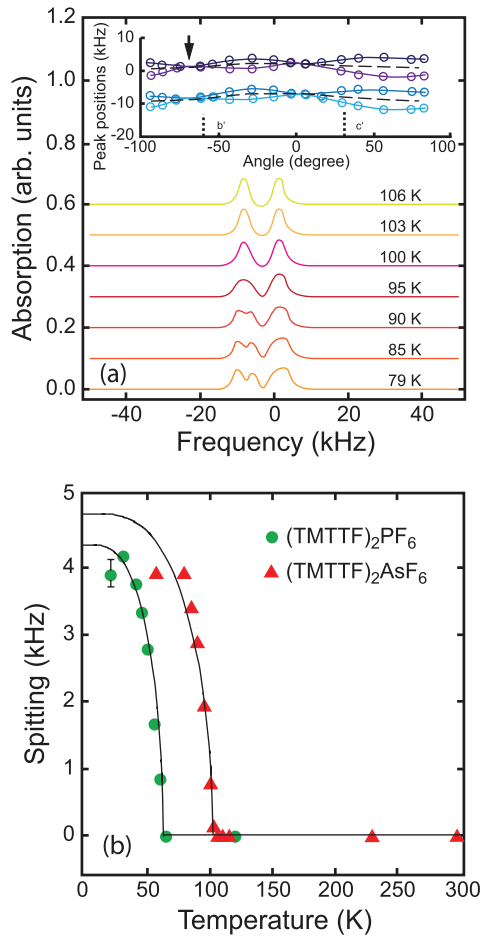


Figure 3. The splitting of the NMR spectral lines at low temperatures evidences charge disproportionation. (a) ^{13}C NMR spectra for $(\text{TMTTF})_2\text{AsF}_6$ recorded at different temperatures. The inset shows the spectrum for a $(b'c^*)$ rotation at $T = 300$ K. The arrow denotes the angle at which the spectra in the main part of the figure were recorded. (b) The temperature dependence of the spectral splitting obtained from one- and two-dimensional NMR spectroscopy for $(\text{TMTTF})_2\text{PF}_6$ and $(\text{TMTTF})_2\text{AsF}_6$ salts. It is a measure of the charge-order parameter below $T_{\text{CO}} = 67$ and 102 K, respectively (after [25]). The lines illustrate the mean-field behavior.

along the molecular stacks (the a -axis) due to electron-molecular vibrational (emv) coupling [29, 30].

The $\nu_{28}(b_{1u})$ stretching mode is antisymmetric and thus infrared active; also, it is considered as a better quantitative probe for the charge disproportionation because the highest charge density of the TMTTF molecule is centered at the outer C=C bonds involved in this vibration. With a linear shift of 80 cm^{-1} per unit charge [32], the charge disproportionation between charge rich and poor sites, $2\delta\rho = \rho_{\text{rich}} - \rho_{\text{poor}}$, is given by

$$2\delta\rho = \frac{\delta\nu_{28}(b_{1u})}{80\text{ cm}^{-1}/e}, \quad (1)$$

where $\delta\nu$ is the difference in frequency positions between the vibration bands associated with the unequal TMTTF molecules; e is the elementary charge.

Albeit in the native crystallographic structure the bonds are already unequal, the CO phase transition involves

significant structural changes which enhance breaking the inversion symmetry in the whole system. In order to yield a net electric dipole moment in the complex system consisting of molecular and anion networks, it is therefore not enough that Coulomb interaction simply creates non-equivalent rich-poor molecular dimer sites in the native structure with dimerized bonds, as previously suggested [33]. Inelastic neutron scattering reveals a $4k_{\text{F}}$ ($q = 0$) distortion due to the shift of the anion lattice along the longitudinal direction (figure 5(a)) [34]. In high-resolution thermal expansion measurements a pre-translational softening of the lattice was observed and attributed to the steric constraints released along the transverse directions because of the longitudinal anion shifts. It is noteworthy that the largest effect happens in the c -direction along which the molecular and anion layers alternate, thus indicating the important role of the anions displacements in the CO phase transition [35, 36]. Based on the unexpectedly large amplitude of the anion shift, Pouget *et al* [37] performed a structural analysis and suggested that the CO phase transformation involves coupling of the TMTTF subsystem with the anion lattice (figures 5(b) and (c)). This aspect of the CO ferroelectric phase transition in $(\text{TMTTF})_2\text{X}$ was recently summarized in [38]. Such an interpretation based on the experimental data is in perfect agreement with theoretical considerations developed independently by Riera, Poilblanc and Brazovskii [21, 40]. They showed that the stabilization of the $4k_{\text{F}}$ bond-CDW order yielding ferroelectricity at long range is a cooperative effect between the Coulomb interaction and coupled TMTTF-anion system. Interestingly, this also affects the magnetic properties and breaks the symmetry, as seen by the rotation of the g tensor and excessive broadening ΔH of the ESR line [41, 42].

2.2. Excitations and collective effects

The dielectric response observed by radio-frequency spectroscopy measurements proves the ferroelectric nature of the CO phase transition and displays features predicted in the theory of conventional ferroelectrics [43–45]; these studies have been summarized by Nad and Monceau [22, 46]. First, a huge Curie-like peak occurs in the real part of the dielectric function $\epsilon' \approx 10^6$ with negligible dispersion, and in the peak of the mean-relaxation time $\tau_0(T)$ right at the phase-transition temperature (figure 6(a)).

Second, the two branches of $1/\epsilon'(T)$ above and below T_{CO} are close to linear, and the slope below is approximately twice that above T_{CO} (figure 6(b)). The loss peaks are Debye-like at temperatures above T_{CO} , while they become broader at lower temperatures; the broadening is caused by an additional relaxation process, which develops in the CO state. This process can be attributed to the response of charged solitons localized within domain walls separating areas of the opposite polarization (figure 7), while the main process—as described above—is due to the collective response of dipoles on TMTTF molecular dimers [44]. As a result the ferroelectric crystal is divided into domains with equivalent polarizations to minimize its total energy; this fact is well-known for conventional ferroelectrics [47]. Even homogeneous and high-quality single

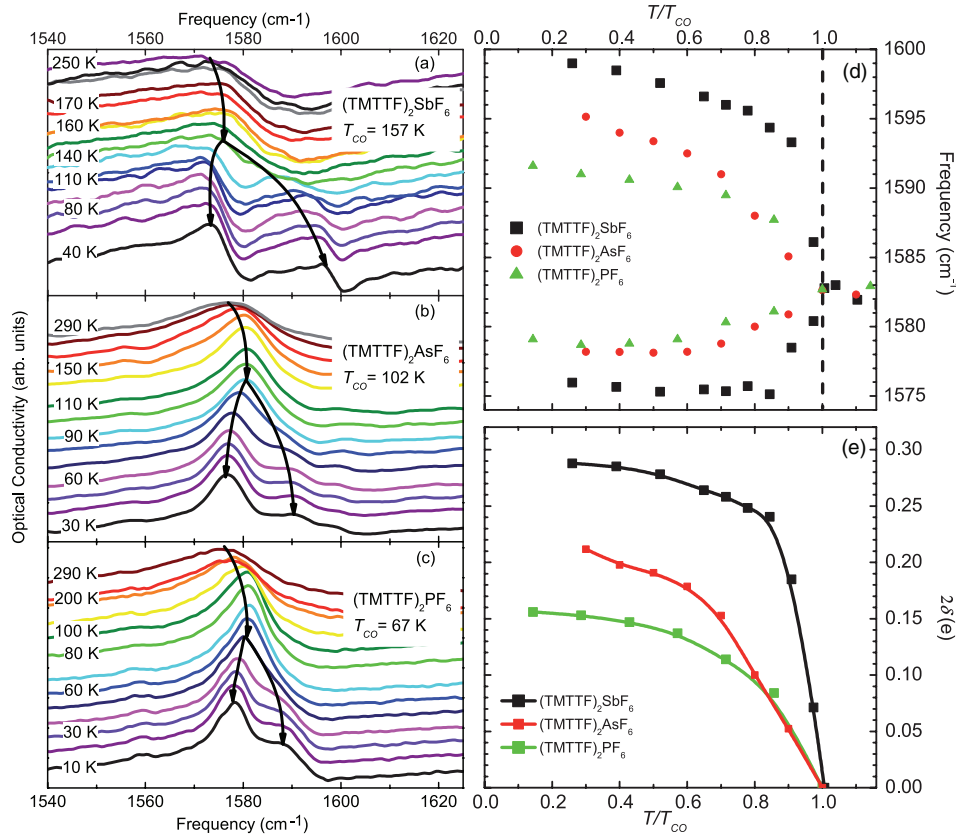


Figure 4. (a)–(c) The optical conductivity of (TMTTF)₂X with the anion X = SbF₆ ($T_{CO} = 157$ K), AsF₆ ($T_{CO} = 102$ K) and PF₆ ($T_{CO} = 67$ K) (top down) recorded along the *c* direction for different temperatures. The conductivity was shifted for clarity. Below T_{CO} , the $\nu_{28}(b_{1u})$ mode splits in two components. (d) Temperature dependence of the split $\nu_{28}(b_{1u})$ mode for (TMTTF)₂X with X = SbF₆, AsF₆ and PF₆. (e) $2\delta(T)$ as estimated from the difference of the two resonance frequencies (after [29, 31]).

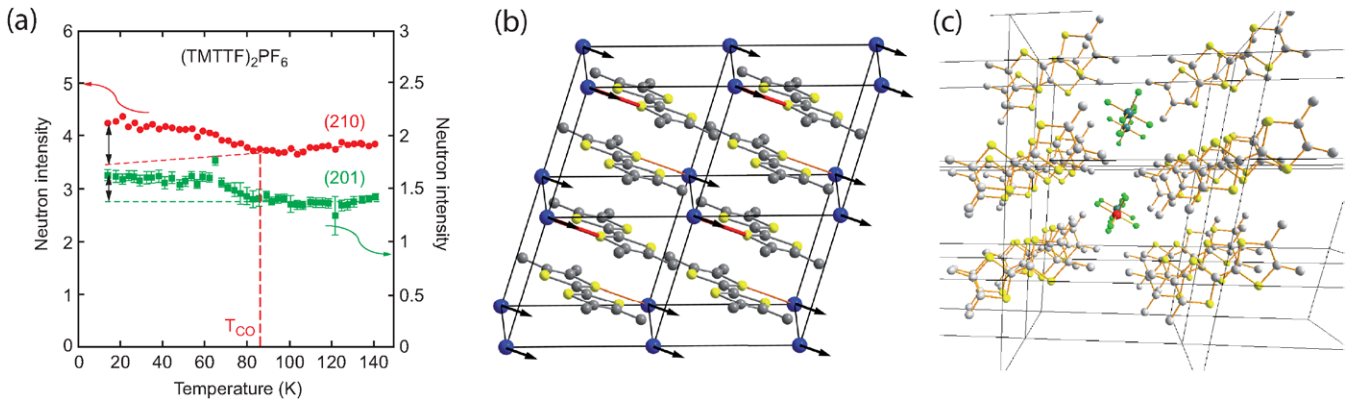


Figure 5. (a) Thermal variation of the peak intensity of the (2 1 0) and (2 0 1) Bragg reflections (red symbols, left axis; and green symbols, right axis, respectively) from neutron scattering experiments on (TMTTF)₂PF₆ crystals (after [34]). (b) Illustration of the anion shifts in the CO phase of (TMTTF)₂X. The anions positioned at the upper part of the unit cell move toward the charge-rich molecule, while the anions at the lower part move away from the charge-poor molecule. The corresponding link to the sulfur atoms are indicated by thick red lines and thin orange lines, respectively. (c) View along the *a*-direction of (TMTTF)₂AsF₆ illustrates the cavity in which the anion is located. Short links exist not only to the terminal methylene groups but also to the sulfur atoms in TMTTF [39].

crystals contain a certain amount of disorder. At high temperatures close to T_{CO} , however, the number of charge carriers is still large enough to screen the electric field at structural boundaries, and thus to eliminate the separation into domains of opposite polarization. We note that the extension of dielectric measurements in frequency and temperature would be worth of doing in order to achieve deeper understanding of

interplay of dielectric processes associated with the domain wall dynamics and collective response of electric dipoles [48].

Another cause of heterogeneity comes from inherent disorder due to the random distribution of anions X in their cavities formed by the TMTTF molecules within the unit cell [39], as sketched in figure 5(c). As a result, the dielectric response of nominally pure single TMTTF crystals resembles that of

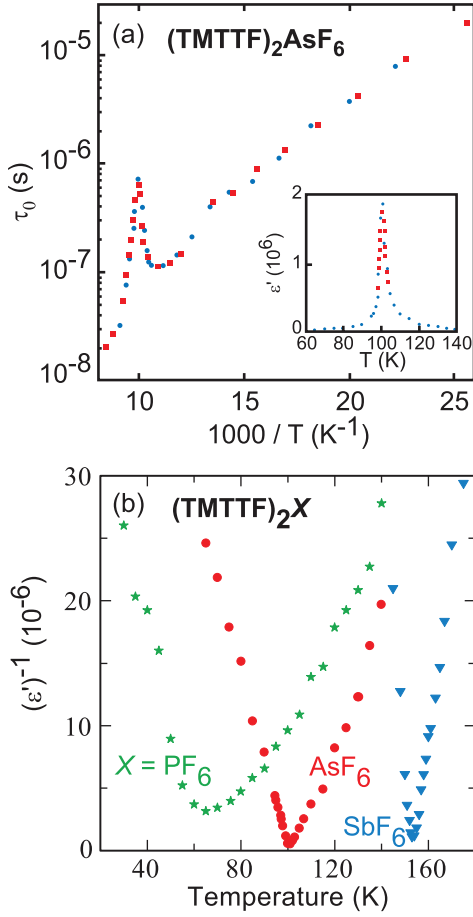


Figure 6. (a) Peak of the mean relaxation time and the real part of the dielectric function at 1 kHz (inset) in the CO phase of $(\text{TMTTF})_2\text{AsF}_6$, (b) Inverse of the real part of the dielectric function in the vicinity of T_{CO} for $(\text{TMTTF})_2\text{PF}_6$, $(\text{TMTTF})_2\text{AsF}_6$ and $(\text{TMTTF})_2\text{SbF}_6$ measured at $f = 100$ Hz (after [43, 44]).

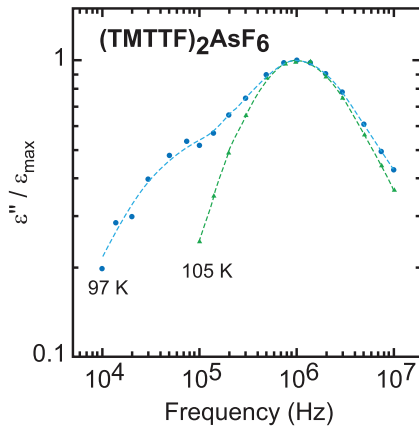


Figure 7. Double logarithmic plot of the frequency-dependent imaginary part of the dielectric function $\epsilon''(\omega)$ of $(\text{TMTTF})_2\text{AsF}_6$ at two representative temperatures above and below T_{CO} . In the CO phase at $T = 97$ K two loss peaks are clearly discernable and can be attributed to the bulk polarization and soliton response, respectively (after [44]).

relaxor ferroelectrics [44, 45]. In previous temperature and frequency dependent dielectric measurements, the peaks of ϵ' and τ_0 were smaller and broader, so that two relaxation processes could not be resolved; nevertheless the dispersion was

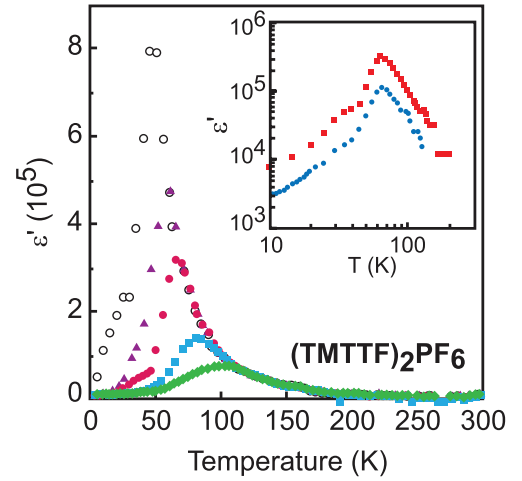


Figure 8. Real part of the dielectric function of a $(\text{TMTTF})_2\text{PF}_6$ single crystal as a function of temperature for different frequencies: open circles, triangles, full circles, squares and diamonds stand for 1, 10, 100, 1000 and 5000 kHz. The inset shows data for two different single crystals at 100 kHz (after [50]).

clearly detected (figure 8). Similarly, the dielectric response in the microwave frequency range indicates the formation of short-range polar order: the dielectric constant is about 40 and the relaxation time strongly decrease below T_{CO} ; the loss part displays a broad anomaly [49].

Let us now consider the simple mean-field approach of non-interacting dipoles to estimate the upper bound of the charge disproportionation $2\delta_p$ within the TMTTF dimer and compare it with the experimentally observed values. From the Curie–Weiss behavior of the measured dielectric constant $\Delta\epsilon = C/(T - T_{\text{CO}})$, we can extract the Curie constant C . It is determined by the number N of dipole moments p per unit cell volume V :

$$C = \frac{Np^2}{V\epsilon_0 k_B}; \quad (2)$$

here ϵ_0 is the permittivity of vacuum and k_B the Boltzmann constant. The dipole moment is given by the charge disproportionation $2\delta_p$ at the intradimer distance d : $p = (2\delta_p)d$. From the experimental data of $\Delta\epsilon$ found in the most homogeneous single crystals of $(\text{TMTTF})_2\text{AsF}_6$, for instance, one obtains $C \approx 2 \cdot 10^6$ K [43]. Taking $N = 2$, $V = 0.598$ nm³, $d = 0.357$ nm, the estimated charge disproportionation $2\delta_p \approx 5e$ is by a factor of ten larger than the upper bound posed by NMR and optical measurements: $2\delta_p \approx 0.26e$ [29]. On the one hand this discrepancy might indicate that the domain walls, rather than the electric dipoles on dimers as widely accepted, are responsible for the observed Curie peak in the vicinity of T_{CO} . On the other hand, the origin of this discrepancy may be in the well documented strong sample dependence of the dielectric constant, which can vary in the range 10^6 – 10^4 . One way to clarify the accuracy of dielectric measurements to estimate the charge disproportionation would be to perform NMR, optical and dielectric measurements on the same single crystal. At the present moment taking into account the overall dielectric data, we are led to conclude that the main dielectric response in the ferroelectric state of $(\text{TMTTF})_2X$ could be ascribed to the collective behavior of dipole moments associated with TMTTF dimers.

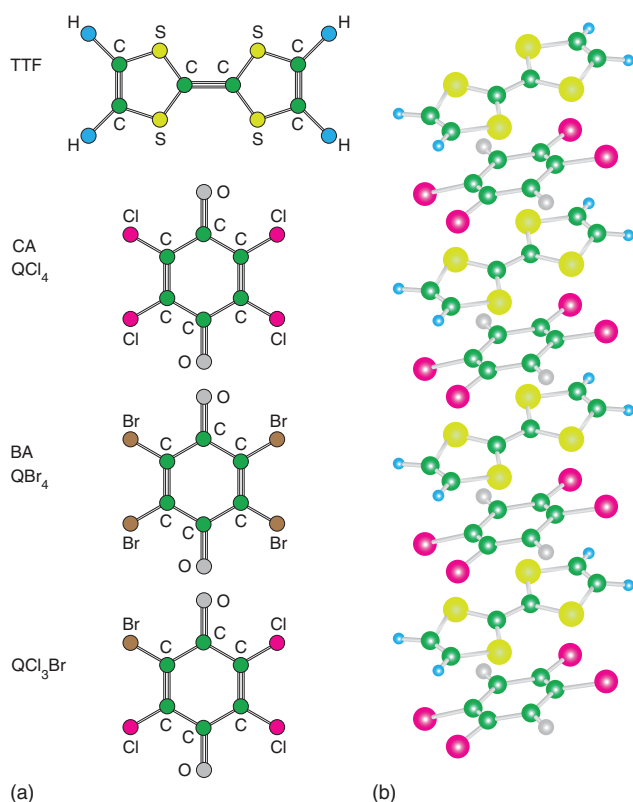


Figure 9. (a) Molecular structure of some of the organic molecules forming mixed stack compounds that undergo a neutral-ionic transition: tetrathiofulvalene (TTF), tetrachloro- *p*-benzoquinone, called chloranil (CA or QCl₄), bromanil (BA or QBr₄) and Br-substituted tetrahalo- *p*-benzoquinones. (b) In the mixed-stack compound TTF-CA the two types of molecule alternate.

3. Neutral-ionic transition in one-dimensional TTF-CA

While most charge-transfer salts discussed in this review consist of segregated stacks of charge donor D and charge acceptor A molecules, there exist also mixed-stack compounds, most prominent TTF-CA. Here TTF or its derivatives together with chloranil or its variants form a single chain by alternating π electron donor and acceptor molecules (... A^{- ρ} D^{+ ρ} A^{- ρ} D^{+ ρ} A^{- ρ} D^{+ ρ} ...) as sketched in figure 9. At ambient conditions, the material is basically neutral ($\rho = 0.2$) but under the influence of pressure ($p_{\text{NI}} = 8$ kbar) or temperature ($T_{\text{NI}} = 81$ K) or photoexcitation TTF-CA becomes ionic. At this first-order neutral-ionic phase transition (NIT) not only the ionicity changes, but dimerization also breaks symmetry that causes formation of ferroelectric domains and a sudden increase of the dielectric constant up to a few hundred. Ferroelectricity is also testified by polarization hysteresis, strong nonlinear effects and ultra-fast optical response.

3.1. Ferroelectric phase transition due to neutral-to-ionic valence instability

X-ray [51] and neutron scattering data [52] taken at different temperatures indicate that the ionic phase is characterized by a dimerization along the stacking direction (figure 10). The

regular ... D A D A D A ... arrangement changes to DA dimers along the stacks; the space group is reduced from $P2_1n$ to Pn , which contains the point group C_s . In other words, inversion and rotation are lost as symmetry operations due to the dimerization. Breaking the symmetry along the stacking direction implies the occurrence of domains with a ... DA DA DA ... or with a ... AD AD AD ... arrangement; both are equally probable if no preferred direction is given externally. As discussed later, the presence of domain walls plays an important role in the ionic phase of TTF-CA. Since adjacent stacks are coupled to some degree, they do not act independently. In addition to the dipole moments of the DA dimers arranged ferroelectrically along the chains below T_{NI} , hydrogen ions form a three-dimensional network of bridges interconnecting the chains. Right after the discovery of these materials, it has been already pointed out by Batail *et al* [54] that the hydrogen bonds are of crucial importance for understanding the neutral-ionic transition.

First evidence for a change in symmetry was obtained from vibrational spectroscopy [55, 56], where in the infrared spectra additional molecular modes appear which are forbidden in the neutral phase. This is surprising since the TTF and CA moieties retain their D_{2h} molecular symmetry at any temperature [57]; only a shift of the modes is expected as the charge on the molecules changes at the NIT. Consequently, Girlando *et al* suggested an advanced model [56, 58] that describes how in the distorted mixed-stack chain the totally symmetric modes of TTF and CA interact with the charge-transfer transition. The vibronic modes basically borrow infrared intensity from the charge-transfer absorption and become both infrared and Raman active at a common lower frequency. It should be noted that this behavior is different from the similar em-coupling process in segregated stacks, where only the infrared modes are affected and move down with respect to the corresponding Raman modes, which remain at the original frequency position [59].

From the observed vibrational frequencies, the degree of ionicity can be estimated in the entire temperature range. For example, the totally symmetric $\nu_5(a_g)$ mode of the CA molecule is not infrared active in the neutral phase and appears only below T_{NI} when the inversion symmetry is broken [56]. In particular, infrared measurements of the charge-sensitive C=O stretching mode $\nu_{10}(b_{1u})$ of the chloranil are utilized to precisely determine the charge on the molecules for any temperature and pressure [60]. Assuming a linear dependence

$$2\delta_\rho = \frac{\delta\nu_{10}(b_{1u})}{160 \text{ cm}^{-1}/e}, \quad (3)$$

it strongly shifts from 1685 cm^{-1} in the neutral CA⁰ to 1525 cm^{-1} in CA⁻. As seen in figure 10(d), ρ increases linearly in the quasi-neutral phase from $0.2e$ at room temperature to $\rho = 0.3e$ right above the neutral-ionic transition at $T_{\text{NI}} = 81$ K [56, 61]. The temperature-induced NIT is the prime example of a first-order transition with a discontinuous jump in ionicity to $\rho \approx 0.5e$ from where it continues to rise as the temperature is reduced further in the quasi-ionic phase until it saturates with approximately $\rho = 0.6e$ [62–67]. Similar conclusions

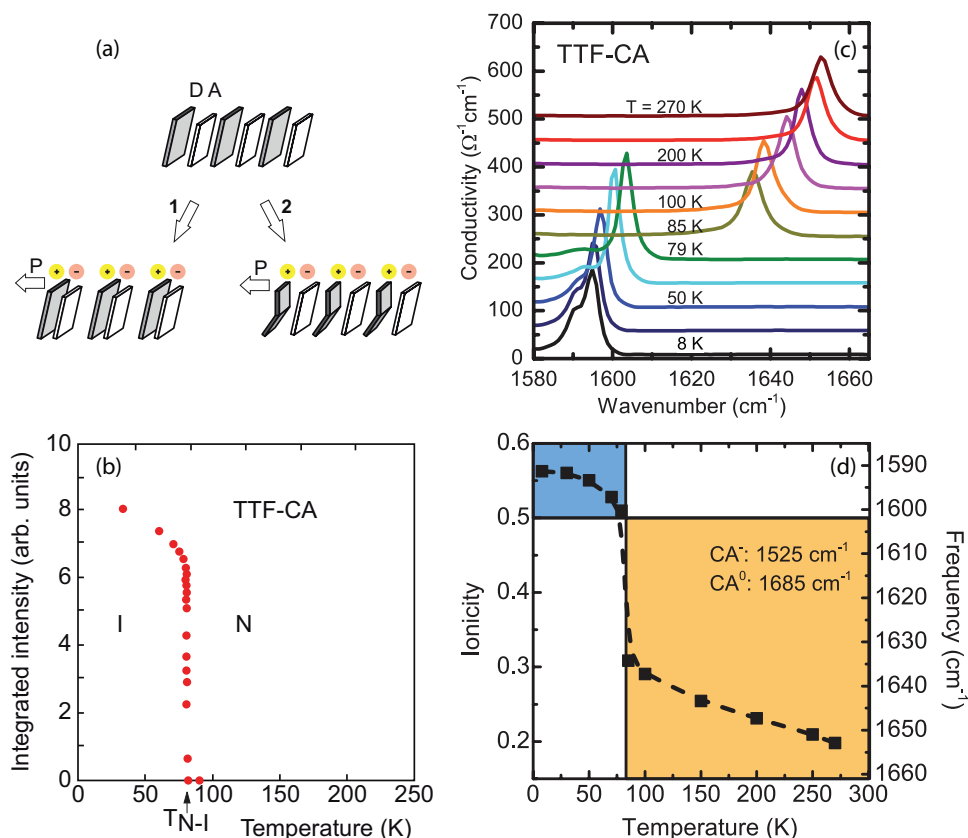


Figure 10. (a) Schematic representation of the mixed-stack structure of TTF-CA creating polar chains by molecular displacement (route 1) or molecular deformation (route 2) for ferroelectricity (after [53]). (b) Temperature evolution of the integrated intensity of the characteristic reflection (0,3,0) obtained by neutron scattering (after [52]). The sudden rise of the (0, k ,0) reflections with $k = 2n + 1$ below T_{NI} and the systematic absence of (h ,0, l) reflections with $h + l = 2n + 1$ in the ionic phase evidence the loss of two-fold screw axis due to dimerization. The structural transition is translation equivalent and takes place at the center of the Brillouin zone; the significant intensity and a Bragg profile indicates long-range order. (c) Optical conductivity of TTF-CA in the frequency range of the C=O stretching vibration of the CA molecule measured for different temperatures with light polarized perpendicular to the stacks. With decreasing temperature the mode shifts to lower frequencies; from the peak position the charge per CA molecule can be determined; the curves are shifted for clarity reasons. (d) The temperature dependence of the ionicity clearly shows the gradual increase of $\rho(T)$ when T is reduced in the quasi-neutral phase (orange shaded). At T_{NI} an abrupt jump is observed; eventually $\rho(T)$ saturates when the temperature is reduced further in the quasi-ionic state (blue shaded). Both experiments clearly rule out any coexistence of phases in the vicinity of the NIT.

are drawn from the shift of the charge transfer band [62–64]. Nuclear quadrupole resonance (NQR) spectroscopy on ^{35}Cl on poly- and single crystalline samples reveal not only a shift in the characteristic lines but also a splitting of the lines upon entering the ionic phase. This confirms the loss in symmetry and change in ionicity [68–71].

3.2. Excitations and collective effects

One-dimensional molecular chains have the tendency towards a Peierls instability, i.e. the lattice becomes distorted and a gap opens at the Fermi energy [17]; this causes a stack dimerization for TTF-CA [72–74]. As the neutral-ionic borderline is approached, a progressive increase in the electronic delocalization is observed along the stack, that amplifies the response of the electronic system to the perturbation from the vibrational degrees of freedom [58]. The Peierls transition in mixed-stack compounds implies the presence of an optically active soft mode [61, 73, 75, 76], in contrast to segregated-stack compounds such as TTF-TCNQ. Following this line of argument, Moreac *et al* [77] and more comprehensively

Girlando and collaborators [61, 76] combined low-frequency Raman and infrared spectroscopy together with a theoretical analysis of the lattice dynamics [75], fluctuation effects and electron–phonon coupling [78]. In the low-energy region up to 100cm^{-1} six Lorentzian peaks could be identified, which show an appreciable frequency shift when the crystal is cooled from room temperature to T_{NI} , as displayed in figure 11. In this range the spectral weight more than doubles upon cooling. The main contribution comes from intermediate modes; in addition the spectral weight is redistributed toward lower-frequency bands [76]. Far-infrared reflection measurements on the related compound TTF-QBrCl₃ yield a similar downshift of the spectral weight as the temperature decreases with an intense peak finally appearing at around 10cm^{-1} just above $T_{NI} = 68 \text{K}$ [79]. In the ionic phase, the feature abruptly disappears. Model calculations of the electronic response to the phonon perturbation [76, 80] nicely reproduce this multi-mode Peierls coupling.

The Peierls mode also causes collective charge oscillations that lead to a strong infrared intensity of the corresponding mode and an enhancement of the dielectric constant. The

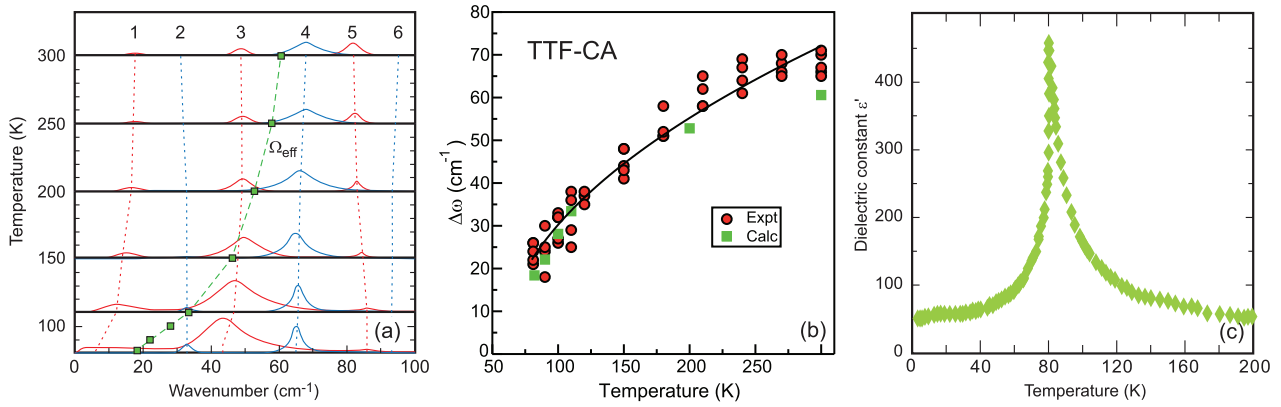


Figure 11. (a) Temperature dependence of the spectra of the six lowest-frequency Peierls coupled phonons, obtained from a fit to the measured reflectivity spectra of TTF-CA; they are labeled ν_1 to ν_6 going from the lowest to the highest frequency. For $T = 300, 250, 200, 150, 110,$ and 82 K the calculated individual Lorentzian bands are also shown. The green squares connected by a dotted line indicate the frequency of the effective Peierls mode (after [76]). (b) Experimental (red circles, [61]) and calculated (green squares) frequency of the effective soft mode in TTF-CA; see [76] for more details. (c) Temperature dependence of the dielectric constant of TTF-CA measured at 30 kHz along the stacking direction (after [65]). The first-order ferroelectric transition at $T_{\text{NI}} = 81$ K is characterized by a Curie–Weiss increase in the paraelectric phase and a discontinuous drop below T_{NI} .

anomaly in the dielectric response was first noticed by Tokura and collaborators [81, 82]: in the paraelectric phase the dielectric constant $\epsilon'(T)$ measured along the chains exhibits a sharp increase (figure 11(c)) that obeys the Curie–Weiss law [65], with a Curie constant of $C \approx 5 \cdot 10^3$ K [83]. The discontinuity below T_{NI} and the thermal hysteresis are evidence for the first-order phase transition. In the case of TTF-QBrCl₃ the anomaly is slightly shifted in temperature and even more pronounced with $\epsilon' = 800$ and $C = 6.4 \cdot 10^3$ K. Further substitution, disorder or pressure, however, cause a complete suppression of the transition [84–87] leading to a quantum phase transition at zero temperature in DM-TTF-QBr_nCl_{4-n}.

The presence of ferroelectric domains could be visualized by electro-reflectance measurements under strong electric fields E of the order of 0.2 – 10 kV cm⁻¹ [88, 89]. Microscopic investigations reveal regions of a certain polarization with a few hundred micrometers in size which grow as the field becomes stronger. Above T_{NI} only a small signal is observed that stems from fluctuations, but it drastically increases in the ionic phase; the development of larger domains is again hindered for temperatures below 50 K. When the field is reversed the domain walls can move, but depinning requires $E > 1$ kV cm⁻¹. This eventually leads to nonlinear electrical transport and switching effects reported by Tokura *et al* [90]. They relate their observation to neutral-ionic domain walls motion. Similarly, the large dielectric response measured in the radio-frequency range is ascribed to the dynamical bound and creeping motion of the solitons separating domains of opposite polarization. Interestingly, also the dielectric constant is significantly reduced upon poling.

Kagawa *et al* [91] observed electric polarization of the TTF-QBrCl₃ crystal when cooled below T_{NI} in an electric field of 0.95 kV cm⁻¹ that changes sign when a field of opposite direction is applied. Similar measurements performed on TTF-CA [83] evidence a ferroelectric polarization of $6.3 \mu\text{C cm}^{-2}$ with a clear hysteresis loop in polarization that closes around 10 kV cm⁻¹ as depicted in figure 12. The remanent polarization is

$P = 6.3 \mu\text{C cm}^{-2}$ and the coercive field $E_c = 5.4$ kV cm⁻¹ at $T = 59$ K. It is interesting to note, that counter-intuitively the positively charged TTF molecules shift towards the positive electrode and the negatively charged CA towards the negative electrode. The net polarization stems from the significant electron transfer within the hybridized orbitals rather than from the ionic displacement as in conventional ferroelectrics [80, 83, 92, 93].

Taking the effective paraelectric moment $p = (2\delta_p)d$ from the Curie constant C , defined in equation (2) or from the remanent polarization P [83], the distance between the anions and cations $d = 0.37$ nm, one dipole ($N = 1$) per unit cell of volume $V = 0.779$ nm³, we yield a charge disproportionation $2\delta_p$, that is a factor of 10–20 larger than the one measured by vibrational spectroscopy, plotted in figure 10(d). A similar discrepancy was observed for the one-dimensional TMTTF salts, as discussed above in section 2.2, but not in the two-dimensional BEDT-TTF system (see section 4.3).

The dynamics of the domain walls at the neutral-ionic transition in TTF-CA was studied in detailed by optical pump-probe experiments combined with Monte-Carlo simulations [67, 94]. The time, temperature and intensity dependences can be modeled by a diffusion-annihilation process of neutral-ionic domain walls. Their random walk explains the relaxation process and its characteristic decay with time (figure 13).

3.3. Ultra-fast dynamics

The neutral-ionic transition in TTF-CA and derivatives is probably the most prominent and best explored light-induced phase transition, certainly in organic compounds [95–98]. From the quasi-ionic state ($\rho > 0.5e$) at $T < T_{\text{NI}}$ the metastable neutral phase can be generated by photo-excitation of charge-transfer states [99–101], when the system is pumped by short laser pulses above the charge-transfer gap of 0.65 eV [64]. Time-resolved reflection

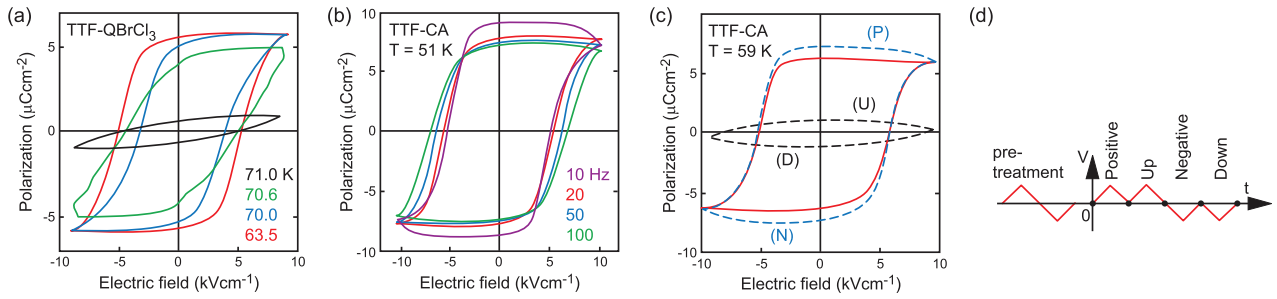


Figure 12. The polarization measured with triangular ac electric field ($E \parallel a$). (a) $P - E$ hysteresis loops of TTF-QBrCl₃ at various temperatures. (b) Hysteresis loops of TTF-CA measured at $T = 51$ K with various frequencies. (c) The $P - E$ curves of TTF-CA using the positive-up-negative-down (PUND) procedure with a double triangular waveform voltage ($f = 500$ Hz, $T = 59$ K) as illustrated on panel (d). The purely hysteresis component (solid curve) was obtained by subtracting the non-hysteresis contributions (up and down runs) from the total ones (positive and negative runs) (after [83]).

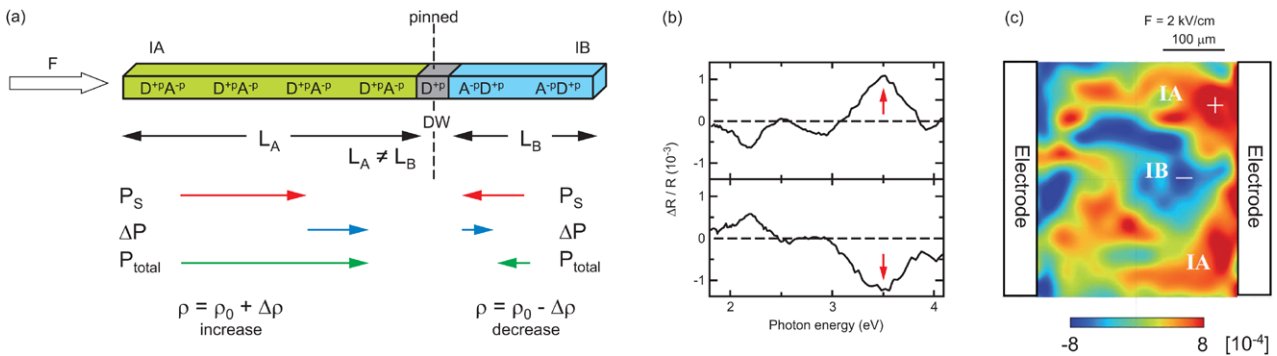


Figure 13. (a) In the ionic phase $T < T_{NI}$ domains of opposite spontaneous polarization P_s develop along the TTF-CA stack, labeled as IA and IB. L_A and L_B indicate the length of the domains. The domain wall is pinned, but can be moved by the application of an electric field, which leads to a change in polarization. (b) Typical infrared spectra of the relative change of reflection $\Delta R/R = [(R_+ - R_0) + (R_- - R_0)]$ between the two opposite directions of electric field of $F = 2$ kV cm⁻¹. The upper and lower panels refer to points (indicated by + and - in panel (c)) measured in the IA and IB domains, respectively. The arrows indicate the measured photon energy in the mapping measurement. (c) Two-dimensional domains in TTF-CA obtained from electro-reflectance measurements at $T = 77$ K (after [89]). Figure used with permission from Kishida *et al* (2009 *Phys. Rev. B* **80** 205201). Copyright American Physical Society.

measurements—with the electric field polarized along the stacking direction—reveal the creation of one-dimensional neutral TTF-CA arrangements within a fraction of a picosecond. They proliferate first forming neutral chains within 20 ps past the excitation and after about 400 ps aggregate three-dimensional neutral domains [102–104]. The structural aspects are studied by time-resolved x-ray scattering and optical investigations of the second harmonic generation [105–108]. Time-resolved infrared vibrational spectroscopy [67, 109] monitors the change in the charge distribution with time. The idea is that a laser pulse creates metastable and neutral domains in the ionic lattice; but the neutral domains quickly relax (1–100 μ s depending on temperature) into the long-living metastable domains with a lifetime of a few hundred microseconds. The size of the domains and details of the dynamics depend on temperature, the laser energy, pulse duration and power.

On top of the timely change of the reflectivity, strong modulations are observed in the picosecond range that are ascribed to coherent oscillations of acoustic and optical lattice phonons [102–104, 110]. These modes have been subject to intense Raman and infrared investigations [61, 75–77] and ascribed to Peierls coupled phonons. For a complete picture

of the thermal and photoinduced neutral-ionic transition, both lattice phonons and molecular vibrations have to be taken into account [111].

Interestingly, also the neutral high-temperature phase can be switched to the ionic state [100, 104]. Using laser pulses as short as 15 fs in order to explore the ultrafast dynamics of charge and molecular degrees of freedom in TTF-CA, Uemura and Okamoto [112] found ionic domains that are photogenerated in the neutral lattice via collective charge-transfer processes (figure 14(b)). In less than 20 fs after one photon is absorbed at $T_{NI} < T = 90$ K, approximately ten donor-acceptor pairs are generated converting about 70% of the neutral states; for higher temperatures, the domain size is reduced [67, 113]. After this purely electronic process, the ionic domains are stabilized by molecular deformations as indicated by fast oscillations of the relative reflectivity (figure 14(a)); this takes about 30–100 fs. Besides these internal molecular modes, the introduced charge transfer between donor and acceptor molecules triggers a dimerization on a slower timescale of 0.6 ps. Eventually this couples the molecular vibrations and leads to a bending to the previously planar molecules accompanied by a charge redistribution [112, 113].

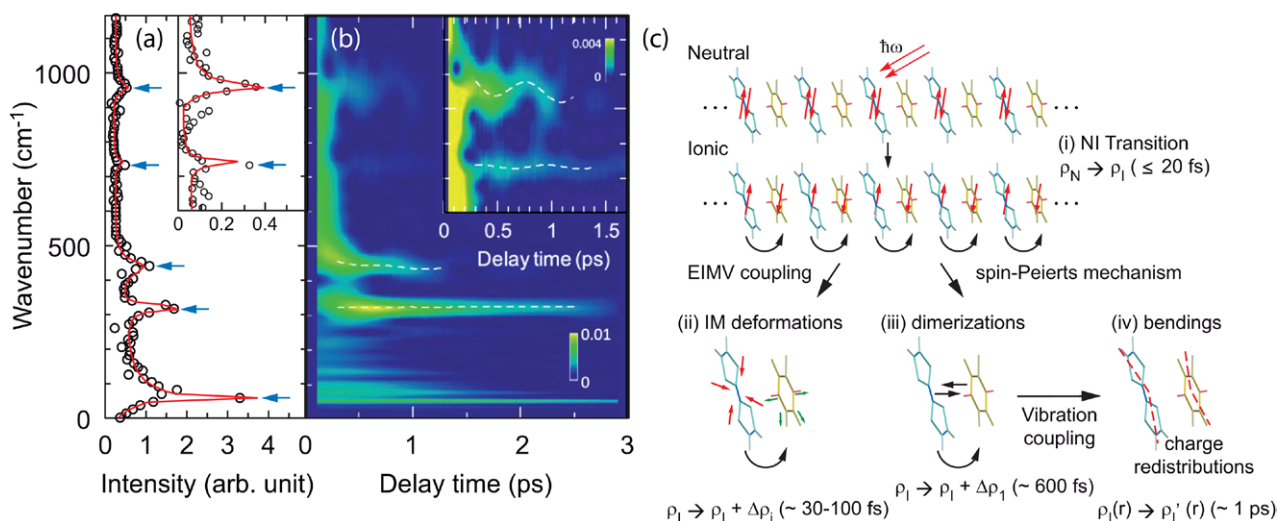


Figure 14. (a) Fourier transform of the oscillatory component (dots) of the relative reflectivity of TTF-CA fitted by a sum of five damped oscillators (solid line). (b) Wavelet transform of the oscillatory component. The broken lines indicate peaks in the Fourier spectra. The $\nu_3(a_g)$ modes of CA at 957 cm^{-1} , the $\nu_3(a_g)$ modes of TTF at 740 cm^{-1} and the $\nu_6(a_g)$ modes of TTF at 438 cm^{-1} show a time dependence of the oscillation frequency modulated by the lattice mode $\nu_p = 53\text{ cm}^{-1}$. (c) The photo-induced transition from the neutral to ionic state of TTF-CA takes place in different steps. Started from purely electronic transitions, molecular vibrations are triggered, that eventually lead to a dimerization of the stacks and charge redistribution. (after [112]). Figure used with permission from Uemura *et al* (2010 *Phys. Rev. Lett.* **105** 258302). Copyright American Physical Society.

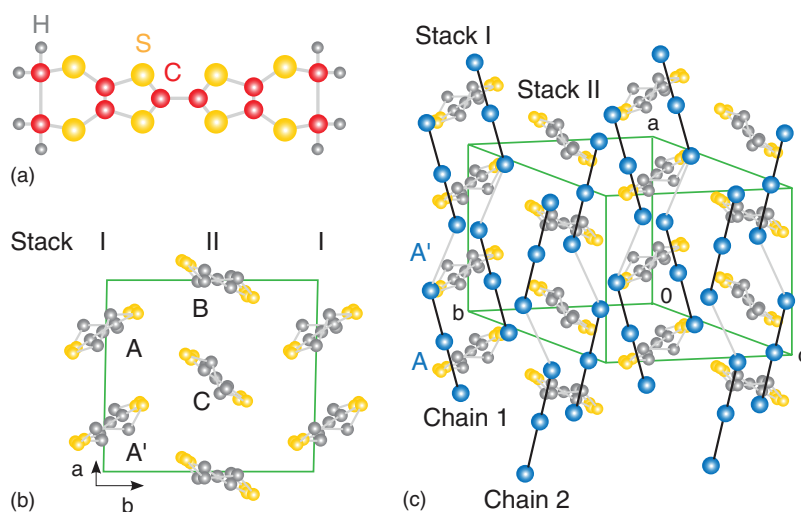


Figure 15. Crystallographic structure of α -(BEDT-TTF) $_2$ I $_3$. (a) Schematic drawing of a bis(ethylenedithio)tetrathiafulvalene molecule, abbreviated BEDT-TTF or ET. (b) Within the (ab) -plane the BEDT-TTF molecules from stacks along a -direction in a herringbone way, with a slight difference between stack I and stack II. The molecules exhibit a triangular arrangement with adjacent stacks. (c) Side view of extended unit cell of α -(BEDT-TTF) $_2$ I $_3$ demonstrates the tilts of the molecules and the chain 1 and 2 of the I $_3^-$ anions.

4. Charge order in two-dimensional α -(BEDT-TTF) $_2$ I $_3$ and θ -(BEDT-TTF) $_2$ RbZn(SCN) $_4$

This section is dedicated to α -(BEDT-TTF) $_2$ I $_3$ and relaxed θ -(BEDT-TTF) $_2$ RbZn(SCN) $_4$, which present the most prominent examples of electronic ferroelectricity due to charge ordering among two-dimensional molecular solids³. At high temperatures, the systems are metallic with an average charge of half a hole per BEDT-TTF molecule. A charge-ordered state develops below the metal-to-insulator phase transition $T_{CO} = 136\text{ K}$ and 190 K , respectively. At T_{CO} the high-temperature symmetry space group changes because the relevant inversion centers are lost, thus resulting in ferroelectricity at

large scales as testified by charge disproportionation, optical second harmonic generation, formation of ferroelectric domains, ultrafast dynamics and characteristic dielectric response.

4.1. Crystallographic and electronic structure

The two-dimensional BEDT-TTF salts consist of alternating anion and cation layers, in which the organic molecules are stacked in a herringbone fashion in the case of the present compounds. The strong coupling between the stacks results in an anisotropic triangular lattice. In α -(BEDT-TTF) $_2$ I $_3$ the organic molecules are arranged in

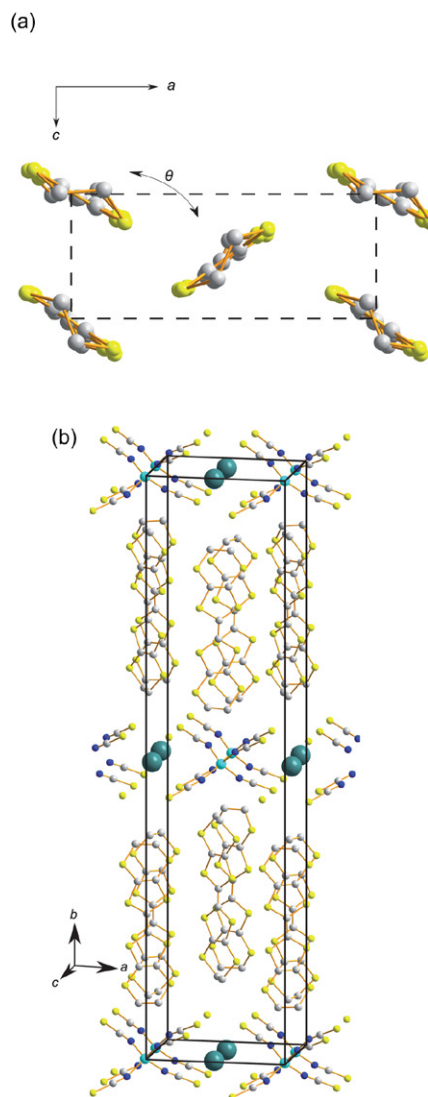


Figure 16. Crystallographic structure of θ -(BEDT-TTF)₂RbZn(SCN)₄. (a) View of BEDT-TTF molecules from one out of two cation layers in the (ac) plane showing their triangular arrangement. (b) Unit cell of θ -(BEDT-TTF)₂RbZn(SCN)₄ containing four BEDT-TTF molecules and two RbZn(SCN)₄ entities.

two crystallographically different stacks I and II extending along the a -axis. Numerous S–S interstack contacts, shorter than the van der Waals distance, occur due to large dihedral angles between BEDT-TTF molecules in neighboring stacks resulting in two-dimensional layers in the (ab) -plane (figure 15(b)) [114]. The anions I_3^- are placed at the crystallographic inversion centers and form zig-zag chains in the a -direction which separate the BEDT-TTF layers along the c -axis (figure 15(c)). The triclinic unit cell (space group $\text{P}\bar{1}$) contains four BEDT-TTF^{0.5+} molecules and two I_3^- anions. Within column I, which is weakly dimerized, BEDT-TTF molecules (denoted as A and A' in figure 15(b)) are related

³ Relaxed θ -(BEDT-TTF)₂RbZn(SCN)₄ is achieved by slow cooling rates smaller than 6 K h⁻¹. It is beyond the scope of this review to discuss the other electronic phases in competition and associated inhomogeneity due to frustrated Coulomb interactions found in θ -(BEDT-TTF)₂RbZn(SCN)₄, which can be tuned in by cooling rate faster than 6 K h⁻¹.

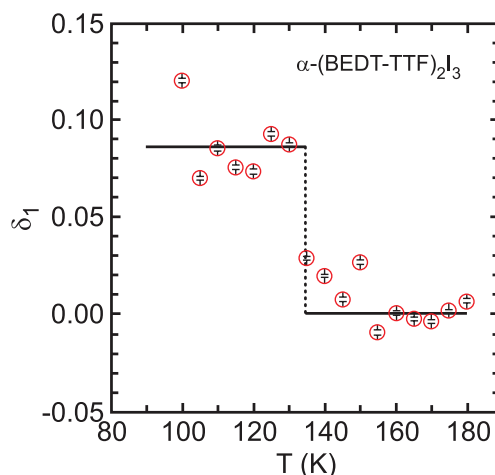


Figure 17. Temperature dependence of the normalized Bragg reflection $(\bar{2}, 8, 6)$ and $(2, 8, 6)$ obtained by x-ray diffraction experiments. The jump in the Bragg intensity $\delta I = [I(hkl) - I(\bar{h}\bar{k}\bar{l})]/[I(hkl) + I(\bar{h}\bar{k}\bar{l})]$ at $T_{\text{CO}} = 136$ K indicates the breaking of inversion symmetry and the formation of an acentric structure in α -(BEDT-TTF)₂I₃ (after [120]).

through an inversion center and thus are equivalent. Column II consists of two different types of molecules placed at the crystallographic inversion centers (denoted as B and C in figure 15(b)) which alternate along the stacks; they are uniformly spaced. At high temperatures the system is characterized by a semi-metallic electronic structure with a Fermi surface containing small electron and hole pockets; this results in a metal-like conductivity within the plane [114–117].

θ -(BEDT-TTF)₂RbZn(SCN)₄ crystallizes in the higher symmetry orthorhombic structure (space group I222) with four BEDT-TTF^{0.5+} molecules and two [RbZn(SCN)₄]⁻ anions per unit cell (figure 16). All BEDT-TTF molecules are crystallographically equivalent and stack along the a -axis. Since the molecules are strongly tilted with respect to each other, there is a large orbital overlap between neighboring stacks leading to a two-dimensional conductivity in the (ac) -plane [118]; in b -direction the layers are separated by the anions as shown in figure 16(b). This two-dimensional RbZn(SCN)₄⁻ network is built from two (SCN)₂ chains, connected by a Rb⁺, in which Zn²⁺ is tetrahedrally coordinated to the SCN⁻ groups. At high temperatures the system is characterized by degenerated bands and a two-dimensional closed Fermi surface with three-quarter filling, resulting in a metallic conductivity behavior within the molecular planes [119].

4.2. Ferroelectric phase transition due to charge ordering

Estimations of the intramolecular bond lengths in α -(BEDT-TTF)₂I₃ infer [120, 121] that already at high temperatures charge disproportionation exists between molecules on sites B and C. At $T_{\text{CO}} = 136$ K charge ordering causes a metal-to-insulator phase transition: the conductivity suddenly drops by several orders of magnitude. The opening of a gap in the charge and spin sector [122, 123] indicates the insulating and diamagnetic nature of the low-temperature state.

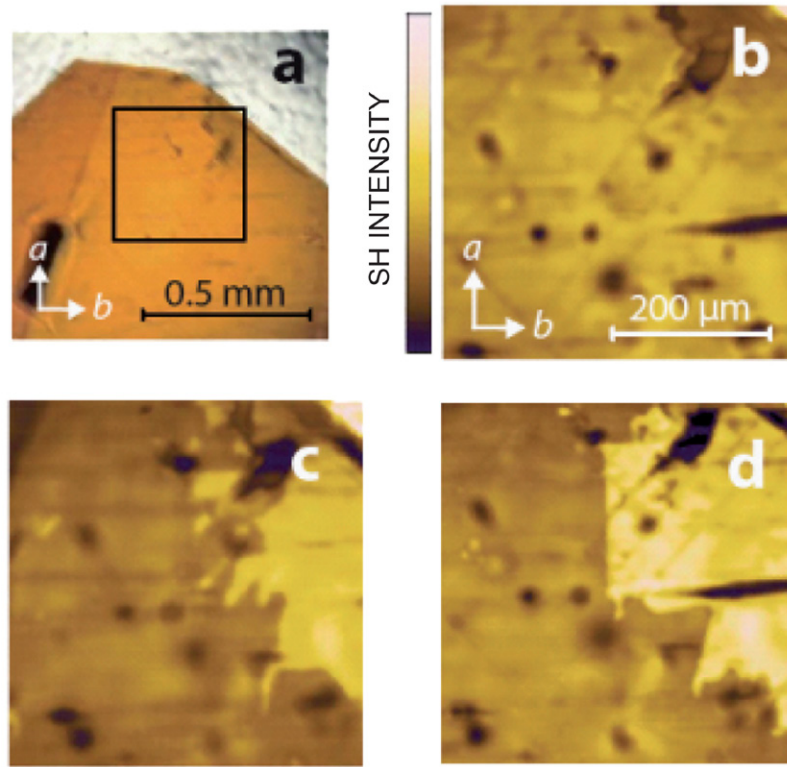


Figure 18. (a) Transmission image of a single crystal of α -(BEDT-TTF) $_2$ I $_3$. Square denotes the area of sample used in second harmonic generation interferometry measurements. (b) and (c) Second harmonic images at representative temperatures 140 K (above T_{CO}) and 50 K (below T_{CO}), respectively. (d) Second harmonic image taken at 50 K after high-temperature annealing; the image reveals that the domains were displaced from the original positions before annealing shown in (c) (figure reproduced with permission from Yamamoto *et al* (2010 *Appl. Phys. Lett.* **96** 122901) [124]). Copyright American Institute of Physics Publishing.

X-ray diffraction measurements [120] show that the symmetry of the space group is reduced from $P\bar{1}$ to $P1$. The structural changes cause a loss of inversion centers between the BEDT-TTF molecules A and A' within column I, the dihedral angles are modified and twin domains are formed due to an acentric structure (figure 17). Interferometry experiments of optical second-harmonic generation allowed Yamamoto *et al* to directly observe large polar domains with opposite polarizations [124]. The domain structure can be easily varied by annealing procedures revealing the mobile nature of the domains (figure 18). The resulting charge disproportionation, deduced from the temperature-dependent intramolecular deformations (figure 19) and modulation of overlap integrals yield the complex electronic pattern as sketched in figure 20. Along the a -axis a $4k_F$ pattern of charge-rich and charge-poor sites develops with molecular charge values ρ at low temperatures: $+0.82e$ and $+0.29e$ within column I, and $+0.73e$ and $+0.26e$ between equally spaced neighboring molecules of column II.

^{13}C -NMR, Raman and infrared vibrational measurements [122, 125–130] directly confirm the charge disproportionation concluded from x-ray diffraction and the presence of horizontal stripes of charge-rich and charge-poor molecular sites. The best local probes are the highly charge-sensitive stretching modes of the BEDT-TTF molecules, such as the symmetric Raman-active ν_3 mode and the asymmetric infrared-active ν_{27} mode of the outer C=C double bonds. The temperature

dependence of the $\nu_{27}(b_{1u})$ is presented in figure 21. With a linear shift of 140 cm^{-1} per unit charge, the charge disproportionation $2\delta\rho$ is calculated by [30]

$$2\delta\rho = \frac{\delta\nu_{27}(b_{1u})}{140\text{ cm}^{-1}/e}, \quad (4)$$

where $\delta\nu_{27}$ is the difference in frequency positions between two ν_{27} vibration bands associated with two non-equal BEDT-TTF molecules [131]. At high temperatures the charge disproportionation within column II is rather small ($2\delta\rho < 0.2e$) (see figure 19). The associated splitting is hidden under a broad band at about 1445 cm^{-1} (figure 21) corresponding to an average charge of $+0.5e$ per molecule; recently Yue *et al* succeeded to resolve the non-uniform site charge distribution within this band [128]. The mode splits abruptly at $T_{CO} = 136\text{ K}$ as it is characteristic for a first-order phase transition; further cooling to low temperatures causes only minor changes. Eventually two pairs of bands are observed at 1415 and 1428 cm^{-1} , and at 1500 and 1505 cm^{-1} , respectively, signaling the formation of four different molecular sites in the unit cell: two non-equally charged molecules within column I and two within column II with $2\delta\rho \approx 0.7e$ and $0.6e$. The lower-frequency bands correspond to approximately $+0.8e$ and $+0.85e$ charge on the molecule, and the upper-frequency bands to $+0.2e$ and $+0.15e$. These values are in full accord with results obtained by the x-ray diffraction measurements, NMR spectroscopy etc.

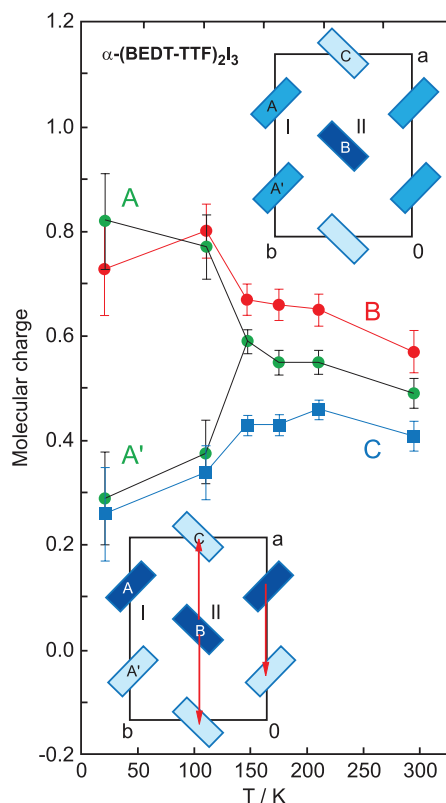


Figure 19. The temperature dependence of charge disproportionation in α -(BEDT-TTF)₂I₃ determined from x-ray diffraction data. Upper and lower insets show charge distribution at molecular A and A' sites (column I), and at B and C sites (column II) at temperatures above and below $T_{CO} = 136$ K, respectively (after [120]).

A careful inspection of figure 20 discloses that the complex CO established in α -(BEDT-TTF)₂I₃ cannot be solely characterized as the horizontal stripe with a 1010 modulation of molecular site charges along the stacking a -axis due to Wigner crystal—like charge localization [132]. In addition to dimerized bonds along the a and b crystallographic directions, it involves the modulation 1100 of site charges and an approximate tetramerization of overlap integrals along two in-plane diagonal directions p_1 and p_2 . The latter suggests the presence of $2k_F$ bond-CDW along the in-plane diagonal directions. Importantly, the bond-CDW concept cannot be associated with ferroelectricity established at $T < T_{CO}$ since no corresponding symmetry-break is observed at T_{CO} .

Notably, ferroelectricity arises only due to breaking the inversion symmetry; this was confirmed by optical second-harmonic generation, where the signal sets in right at T_{CO} and develops gradually with decreasing temperature (figure 22) [133]. It is important to realize that the symmetry is broken because the molecules A and A' of column I lose their inversion centers; thus the net-dipole moment is generated (the case shown in figure 1(d)). Conversely, the equivalent bonds within column II result in a cancellation of the electric dipoles between charge-rich and charge-poor neighboring molecules (see figure 1(b)).

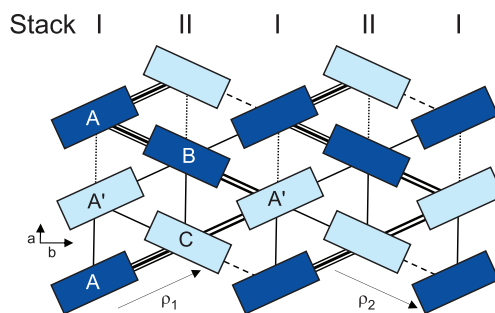


Figure 20. Schematic representation of a $2k_F$ bond-charge density wave established in α -(BEDT-TTF)₂I₃. Full and open rectangles denote charge-rich and charge-poor molecular sites (after [122]). Different lines indicate relative magnitudes of overlap integrals as deduced from x-ray data using extended Hückel molecular orbital calculations by Kakiuchi *et al* [120]. p_1 and p_2 indicate the diagonal directions. The same charge order pattern, but with no modulation of overlap integrals along stripes, is established in θ -(BEDT-TTF)₂RbZn(SCN)₄ at low temperatures.

A similar charge order, involving the change of the high-temperature space group and the loss of some inversion symmetry centers, was also found in the relaxed state of θ -(BEDT-TTF)₂RbZn(SCN)₄. Short-range CO develops at high temperatures and a phase transition sets in at $T_{CO} = 190$ K [119, 134, 135]. Structural changes, much larger than observed in α -(BEDT-TTF)₂I₃, involve the reduction of the symmetry space group from I222 to P2₁2₁2₁ resulting in the loss of inversion centers between BEDT-TTF molecules, the doubling of the unit cell along the in-plane c -axis and changes in dihedral angles [119, 135, 136]. ¹³C-NMR, Raman and infrared spectroscopy as well as x-ray structural measurements all have revealed the formation of horizontal charge stripes along the a -axis with a charge-rich and charge-poor $4k_F$ pattern along the c -axis: $+0.8e : +0.2e$ on two non-equal BEDT-TTF molecules A and B within dimers stacked in two columns in the unit cell (figure 23) [26, 137–141]. An extensive account on charge-sensitive Raman and infrared vibrational modes associated with the CO fluctuations in the metallic phase and the CO ordering in θ -(BEDT-TTF)₂RbZn(SCN)₄, as well as in α -(BEDT-TTF)₂I₃ can be found in [30, 142].

It is noteworthy that basically the same CO pattern is established in θ -(BEDT-TTF)₂RbZn(SCN)₄ as it is in α -(BEDT-TTF)₂I₃ (see figure 20). Importantly, in contrast to the ferroelectricity observed in α -(BEDT-TTF)₂I₃, the net-dipole moment due to the electric dipoles on BEDT-TTF molecular dimers is generated within both BEDT-TTF columns in the unit cell (the case shown in figure 1(d)). Another distinction concerns the CO pattern: there is no modulation of bonds between molecules within the stripes yielding an uniform Heisenberg coupling between spins. Consequently, no gap opens in the spin sector at T_{CO} and the system behaves as a paramagnetic insulator down to the spin-Peierls phase transition at 30 K where it enters into the spin-singlet phase [119, 132, 137]. Notably, while the bonds along the two diagonal

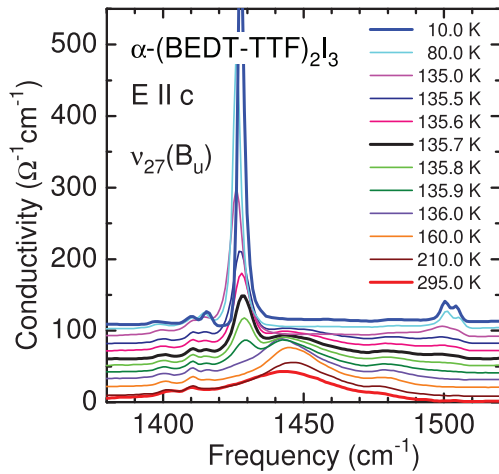


Figure 21. Splitting and shift of antisymmetric outer C=C double bond $\nu_{27}(b_{1u})$ stretching mode in the CO phase of α -(BEDT-TTF) $_2$ I $_3$ as the temperature is reduced below $T_{CO} = 136$ K (after [122]).

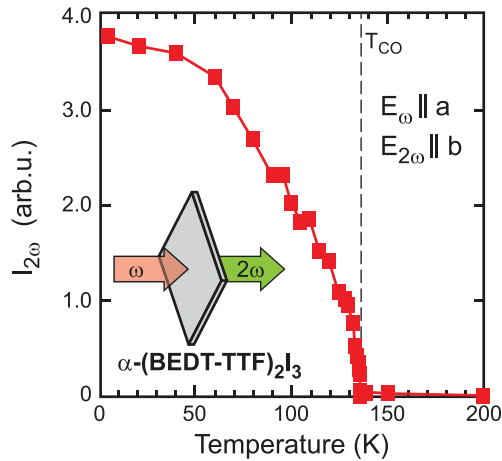


Figure 22. Temperature dependence of the ferroelectric order parameter in α -(BEDT-TTF) $_2$ I $_3$ probed by the optical second harmonic generation (after [133]).

in-plane directions are dimerized in the paramagnetic CO phase, they become tetramerized in the singlet phase, similarly as they are in the CO state of α -(BEDT-TTF) $_2$ I $_3$.

Using numerical many-body calculations Clay, Mazumdar and collaborators developed a theoretical approach for θ -(BEDT-TTF) $_2$ RbZn(SCN) $_4$ that includes electron–electron and electron–phonon interactions [143]; it also turned out to be the most adequate model to describe the CO phase in α -(BEDT-TTF) $_2$ I $_3$. The theory successfully reproduces the experimentally established CO pattern in these two systems; the surprising result is that the only relatively small electron–phonon interaction has to be included to form horizontal stripes with bond dimerization perpendicular to them and bond tetramerizations along the two diagonal in-plane directions. Thus, in this scenario, the horizontal stripe phase is accompanied by a two-dimensional bond-CDW; see Ivek *et al* [122] for a detailed discussion.

Finally, we comment on the nature of the CO-driven ferroelectricity in α -(BEDT-TTF) $_2$ I $_3$ and θ -(BEDT-TTF) $_2$ RbZn(SCN) $_4$. A purely electronic mechanism has been

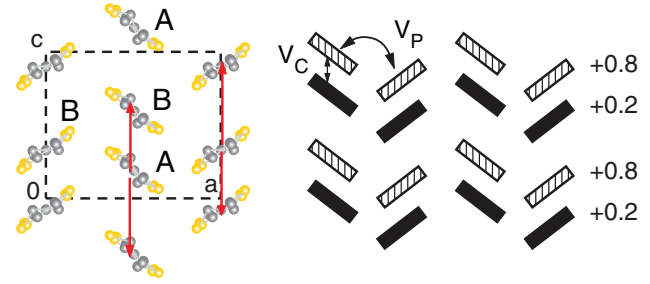


Figure 23. Schematic representation of cation layer in θ -(BEDT-TTF) $_2$ RbZn(SCN) $_4$ in the CO state. The molecules are slightly dimerized along the chains; here A denotes charge-rich, while B denotes charge-poor molecules (following [135, 140]).

developed, including on-site and inter-site Coulomb interactions, suggesting the formation of a Wigner-crystal-like phase [2, 132]. It is experimentally supported by strong non-linear effects and ultra-fast dynamics. However, these findings, as well as theoretical considerations of ultra-fast phenomena indicate that electron–phonon coupling cannot be neglected to explain the observed effects (see section 4.3). In addition, calculations based on the density functional theory (DFT) suggest that the CO-driven ferroelectricity in α -(BEDT-TTF) $_2$ I $_3$ is amplified by anion interactions [37, 117]. Namely, no significant changes in the wave vector dispersion of the band structure below T_{CO} was found, thus indicating possible modifications of local anion–cation interactions; even small displacements of anions toward (away) the charge-rich (charge-poor) molecules would increase (decrease) hydrogen bonding between anions and BEDT-TTF molecules and thus enhance the charge disproportionation. Hence, similarly as in the case of CO in (TMTTF) $_2$ X (see section 2), this approach emphasizes the importance of cooperative actions between Coulomb interactions and coupled cation (BEDT-TTF)–anion subsystems for the stabilization of electronic ferroelectricity.

4.3. Excitations and collective effects

Extensive measurements of the dielectric response have been performed on α -(BEDT-TTF) $_2$ I $_3$ over the last 20 years [122, 144–147]. Within the molecular planes the dielectric spectra consist of two relaxations (figure 24(a)), which are related to the complex CO pattern (see figure 20). The response associated with the presence of two-dimensional bond-CDW along the two in-plane diagonal directions p_1 and p_2 possesses a large dielectric constant ϵ' and is thermally activated. Due to that only below approximately 75 K another much smaller dielectric mode can be detected, which is associated with ferroelectricity (figure 24(b)). A more detailed discussion can be found in [122, 145].

Here we focus on the smaller dielectric mode that is directly related to the ferroelectric nature of the low-temperature phase. The observed response is described by the generalized Debye function

$$\epsilon(\omega) - \epsilon_{HF} = \frac{\Delta\epsilon}{1 + (i\omega\tau_0)^{1-\alpha}}, \quad (5)$$

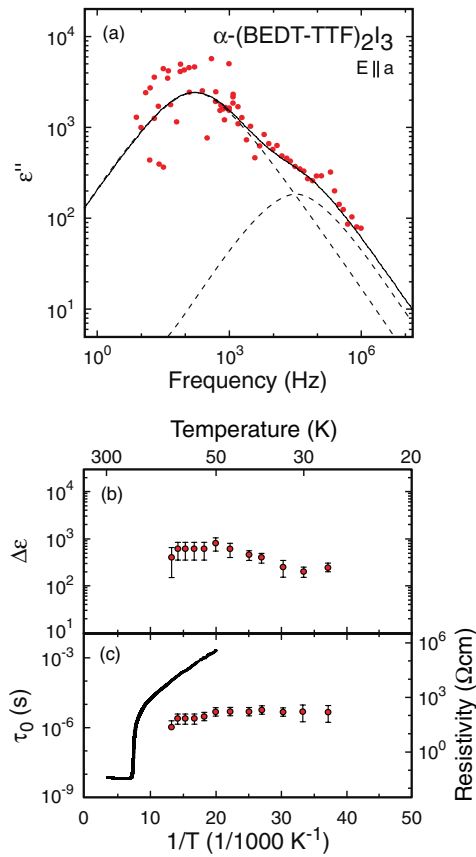


Figure 24. (a) Double logarithmic plot of the frequency dependent imaginary part of the dielectric function $\epsilon''(\omega)$ in α -(BEDT-TTF) $_2$ I $_3$ for direction $\mathbf{E}||a$ at a representative temperature of $T = 47$ K well into the charge-ordered state. At $T < 75$ K two dielectric relaxation modes are observed as indicated by the dashed lines; the full curve represents a fit to a sum of two generalized Debye functions. (b) In-plane dielectric strength and (c) mean relaxation time of the dielectric mode associated with ferroelectricity as a function of inverse temperature. The dc resistivity (right axis) is represented with a full line (after [122]).

where $\Delta\epsilon = \epsilon_0 - \epsilon_{\text{HF}}$ corresponds to the strength of the mode; ϵ_0 and ϵ_{HF} relate to the dielectric constant in the static and high-frequency limit, respectively; τ_0 is the mean relaxation time; and $1 - \alpha$ is the symmetric broadening of the relaxation time distribution function. In α -(BEDT-TTF) $_2$ I $_3$ this mode is characterized by $\Delta\epsilon \approx 400$, by the broadening parameter $1 - \alpha \approx 0.7$ and by the temperature-independent mean relaxation time (figures 24(b) and (c)). This non-dispersive mode, observed for $\mathbf{E}||a$ and $\mathbf{E}||b$, can be ascribed to the motion of the domain walls created between twinned domains of opposite ferroelectric polarization, whose presence below T_{CO} is experimentally evidenced as explained in section 4.2.

The constraint of charge neutrality⁴ suggests two types of domain wall pairs, as sketched in figure 25. The first type is given by considering the a -axis: the domain walls' interior have to contain both charge signs (figure 25(a)). The second type is a pair of domain walls, consisting of a domain wall and the corresponding anti-domain wall between charge-rich and charge-poor stripes along the b -axis (figure 25(b)). In dielectric measurements an external ac electric field applied along

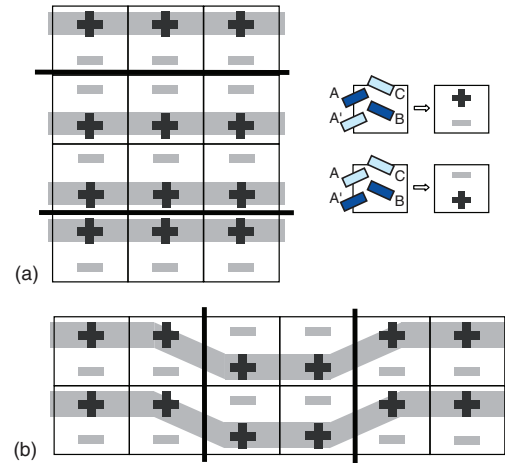


Figure 25. Two different types of domain wall pairs in the charge-ordered phase of α -(BEDT-TTF) $_2$ I $_3$. (A, B)- and (A', B)-rich unit cells are represented as + - or - + cells which form charge stripes. For simplicity B and C molecules are omitted. Gray thick and thin black lines stand for charge-rich stripes and a domain wall pair, respectively (after [122]).

the a -axis couples to the dipole moments on the dimerized A and A' molecules (column I) of each unit cell. Thus the symmetry between two dipole orientations is broken; and due to first-neighbor interactions the dipoles can be easily flipped at the domain boundary. Coupling to a field along the b -axis which is effectively perpendicular to AA' dipoles, although less apparent, can be understood by invoking the interaction between dimerized molecules A and A' in column I, with molecules B and C in column II. At the energetically unfavorable domain boundary B and C molecules effectively couple AA' dipoles to perpendicular external fields and allow for the domain-wall motion along the b -axis as well.

The domain-wall motion is expected to depend on the interaction with defects that might be randomly scattered in the crystal, resulting in a broad distribution of relaxation times, just as observed. It indicates that the dielectric relaxation happens between different metastable states, which correspond to local changes of the charge distribution across the length scale of the domain-wall thickness. A nearly temperature-independent mean relaxation time evidences that resistive dissipation cannot be dominant for domain-wall pairs, at least far below T_{CO} , and that the dielectric relaxation is governed by low energy barriers. The magnitude of $\epsilon \approx 400$ provides additional support for the assignment of these excitations to domain-walls because their dynamics is commonly characterized by the dielectric constants of the order of 1000 or less (see sections 2.2 and 3.2). Its amplitude is almost temperature independent, indicating that the number of domain walls does not change on cooling as expected in acentric crystals.

Since the accessible frequency window is experimentally restricted [122, 145], the Curie-like peak of $\epsilon(\omega)$ (and the maximum in $\tau_0(T)$) could not be identified for α -(BEDT-TTF) $_2$ I $_3$, in contrast to the ferroelectric phase transition in TMTTF and TTF-CA compounds discussed in sections 2.2 and 3.2. When looking at the temperature dependence of the

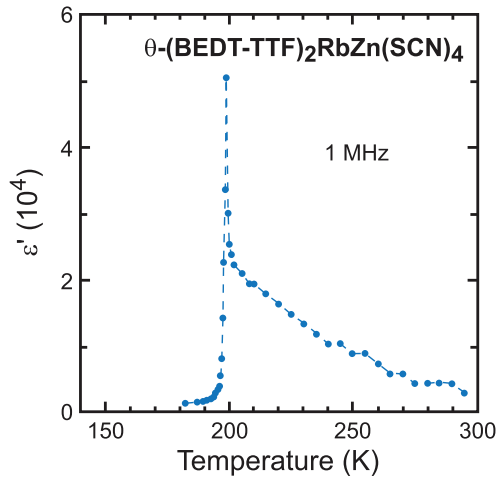


Figure 26. Temperature dependence of the real part of the dielectric function (ϵ') measured in θ -(BEDT-TTF)₂RbZn(SCN)₄ at a frequency of 1 MHz for $\mathbf{E} \parallel c$ (after [149]).

in-plane dielectric response at 2 MHz, however, a large Curie-like peak of the dielectric function is observed with $\epsilon' \approx 10^5$ at the CO phase transition $T_{CO} \approx 140$ K [144, 148]. A similar observation was made for θ -(BEDT-TTF)₂RbZn(SCN)₄ at $T_{CO} \approx 200$ K (figure 26), where the mode is smaller and exhibits no dispersion [149]. When T_{CO} is approached from high temperatures, $\epsilon'(T)$ steadily increases because short-range charge inhomogeneity is present, in accord with NMR and x-ray measurements (see section 4.2). A coexistence of metallic and insulating islands above T_{CO} was suggested by frequency-dependent measurements of the out-of-plane dielectric function [150].

It is interesting to note, that ϵ' displays no dispersion in the vicinity of T_{CO} , while it becomes weakly frequency dependent at lower temperatures. From the Curie–Weiss behavior, although valid only for independent dipoles (see section 2.2), we may extract the Curie constant and estimate the charge disproportionation within the molecular dipoles. From the available experimental data of $\Delta\epsilon$ for α -(BEDT-TTF)₂I₃ [148] the Curie constant is $C \approx 6.6 \cdot 10^4$ K. Using $N = 2$ (molecules at A and A' sites only), $V = 1.6395$ nm³, $d = 0.41$ nm in equation (2), we get $2\delta_p \approx 1e$. The same approach applied to θ -(BEDT-TTF)₂RbZn(SCN)₄ [149] gives the Curie constant $C \approx 2 \cdot 10^4$ K and taking $N = 4$, $V = 2021$ nm³, $d = 0.465$ nm, it yields $2\delta_p \approx 0.49e$. Although these estimates are rather crude, they correspond reasonably well to the charge disproportionation $2\delta_p \approx 0.6$ – $0.7e$ measured by NMR and optical spectroscopy. We recall that similar estimates did not work out for the one-dimensional TMTTF and TTF-CA systems, as discussed in sections 2.2 and 3.2.

Another experimental fingerprints of the ferroelectric domain wall motion comes from a huge negative differential resistance and reversible switching to transient high-conducting states, which has been observed in α -(BEDT-TTF)₂I₃ by dc electric-field-dependent pulse measurements [151]. The negative differential resistance sets in above the threshold

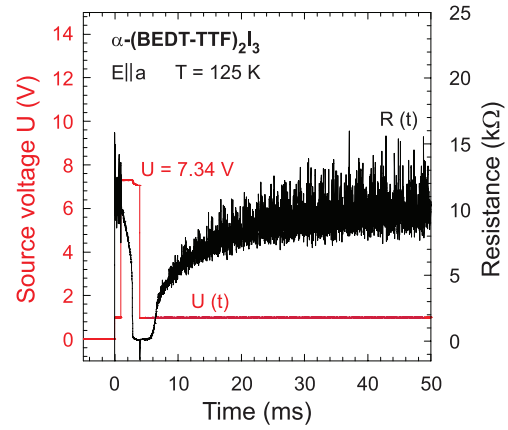


Figure 27. Effect of a sufficiently high dc electric field applied along the a -axis in the CO state of α -(BEDT-TTF)₂I₃ at a representative temperature $T = 125$ K. The application of an initial 3 ms high-field pulse (red) drives the sample metallic; after 2 ms it decays back to the initial high-resistance state in a single-exponential manner (after [151]).

field E_{th} and is accompanied with a significant change in shape of the measured resistivity $R(t)$ in time, which critically depends on the applied measurement mode. When the constant-voltage mode is used, the $R - t$ curves show a discontinuous jump to a low-resistance state. Delay times become longer for fields close to the threshold indicating the field-dependent formation of the connected metallic-like regions. The results shown in figure 27 suggest domain walls, whose rate of formation strongly increases at high applied dc electric fields and overcomes their formation due to thermal excitations. Subsequently, the motion of domain wall pairs become increasingly correlated and thus creates growing conduction regions until percolation promotes negative differential resistance. The time-dependent effects can be associated with a modification of coupling between cation and anion sublattices, involved in the CO phase transition, which are induced by the applied electric field [117].

4.4. Ultra-fast dynamics

Let us now address experiments on the optical nonlinearity and ultrafast photo-response of the charge-ordered state using time-resolved femtosecond pump and probe spectroscopy; the observations strongly support a purely electronic mechanism of the ferroelectricity in α -(BEDT-TTF)₂I₃ and in the relaxed θ -(BEDT-TTF)₂RbZn(SCN)₄. Iwai and collaborators [133, 152–155] found that CO is destroyed by an initial femtosecond laser pulse, macroscopic metallic domains are formed within 15 fs, and eventually they relax back to the CO state within some picoseconds or nanoseconds. This fast relaxation is clearly different from the one at the millisecond time scale observed when a high dc electric field is applied. Figure 28 shows the transient reflectivity spectra $\frac{\Delta_T R}{R} = \frac{R' - R}{R}$ measured at a delay time of 0.1 ps after the excitation pulse of $\hbar\omega = 0.89$ eV. It very much agrees with the thermal change of the reflectivity spectra $\frac{\Delta_T R}{R} = \frac{R(T > T_{CO}) - R(T < T_{CO})}{R(T < T_{CO})}$. The fact that the

⁴ Charge neutrality constraint implies a change of stripes equivalent to strictly replacing unit cells of one twin type with another.

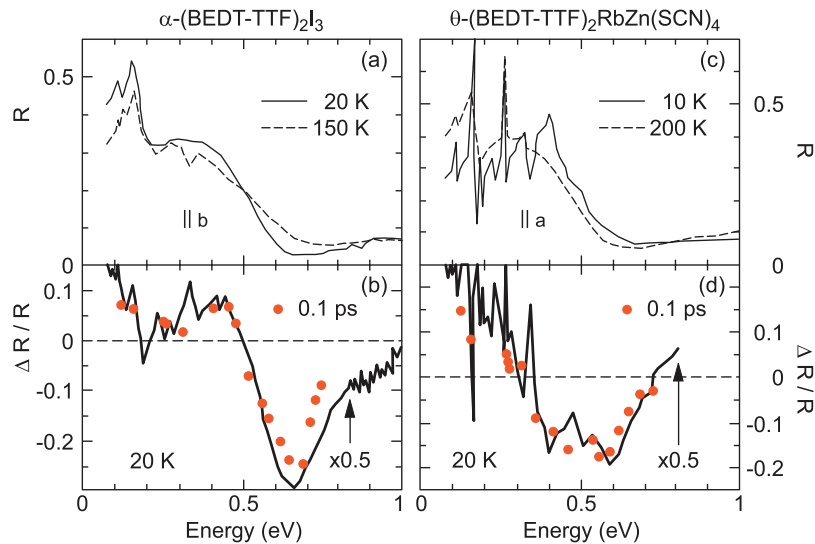


Figure 28. ((a), (b)) Reflectivity spectra of α -(BEDT-TTF) $_2$ I $_3$ (left frame) and θ -(BEDT-TTF) $_2$ RbZn(SCN) $_4$ (right frame) at temperatures well above (dashed lines) and below (solid lines) the transition temperature T_{CO} . In panels (b) and (d) the red dots indicate the photoinduced reflectivity change $\Delta_T R/R$ measured 0.1 ps after the pump pulse at $T = 20$ K. The solid curve correspond to relative change of the reflectivity spectra above and below the charge-order phase transition $\Delta_T R/R$ (after [152]).

charge-ordered state melts extremely fast on a sub-picosecond time scale indicates that the initial process is purely electronic and no structural instability is associated with it [153].

The decay process in α -(BEDT-TTF) $_2$ I $_3$ typically occurs in the picosecond range and strongly depends on temperature T and light intensity I_{ex} : a significant slowing-down is observed when the temperature rises close to T_{CO} suggesting an inhomogeneous character of the photo-induced metallic state. While for low intensities, these microscopic metallic domains relax rapidly to the charge-ordered insulating state, for high laser intensities they condense into macroscopic domains, associated with some molecular rearrangement [156, 157]. It is known from the thermally driven charge-order transition that for α -(BEDT-TTF) $_2$ I $_3$ this structural modification is very small [116, 120, 144, 158]; in contrast to θ -(BEDT-TTF) $_2$ RbZn(SCN) $_4$ where the symmetry of the molecular arrangement is significantly broken at T_{CO} due to a rotation of the organic molecules [118, 135, 159]. The reduction of the structural symmetry in the charge-ordered phase of θ -(BEDT-TTF) $_2$ RbZn(SCN) $_4$ modulates the intermolecular charge transfer. While in α -(BEDT-TTF) $_2$ I $_3$ the excited electrons condense to a macroscopic metallic state, in θ -(BEDT-TTF) $_2$ RbZn(SCN) $_4$ a large potential barrier against the molecular rotation prevents this condensation into semi-macroscopic quasi-stable metallic domains; the latter compound returns to the CO state within a few picoseconds as demonstrated in figure 29.

This problem was studied numerically by employing exact many-electron wave functions coupled with phonons in the extended Peierls–Hubbard model on an anisotropic triangular lattice [156]. The calculations yield only a quantitative difference in the photo-induced dynamics, confirming that they originate in the different crystallographic symmetry. In particular, it was found that the CO melting in θ -(BEDT-TTF) $_2$ RbZn(SCN) $_4$ requires a larger photo-absorption, in accord with the experimental findings. The high symmetry

causes charge frustration yielding quasi-degeneracy among electronic states with different CO patterns in metallic state in the absence of lattice distortions. On the other hand, in the low-symmetry α -(BEDT-TTF) $_2$ I $_3$ system, this problem is avoided and thus the charge disproportionation without lattice changes can even exist in the metallic state (see figure 19).

Finally, we note that no polarization switching by an applied electric field has been reported until now, which may be due to experimental difficulties related to either relatively high conductivity, or to a low breakdown field.

5. Ordering in two-dimensional κ -(BEDT-TTF) $_2$ X

κ -(BEDT-TTF) $_2$ Cu[N(CN) $_2$]Cl (often abbreviated as κ -Cl) and κ -(BEDT-TTF) $_2$ Cu $_2$ (CN) $_3$ (abbreviated as κ -CN) are two-dimensional dimer Mott insulators, in which the BEDT-TTF molecules form face-to-face dimers arranged in a triangular lattice as depicted in figure 30(b). The field of electronic ferroelectricity was boosted by the theoretical exploration of quantum electric dipoles on molecular dimers interacting via dipolar-spin coupling. The possible competition between magnetic and charge-ordered phases has received enormous attention and it was suggested that a paired electron crystal forms due to frustration-induced charge disproportionation [4, 163–165]. Despite considerable experimental efforts worldwide, until now no structural changes have been identified that are required for a broken symmetry, and no spectroscopic evidence has been found for charge disproportionation (figure 31) or the presence of electric dipoles [166, 167]. Nevertheless, anomalous lattice effects, electric polarization switching, anomalous dielectric, microwave and optical response were discussed in favor of charge-order-driven ferroelectricity [168–173]. In order to reconcile these seemingly opposite findings alternative approaches were developed most

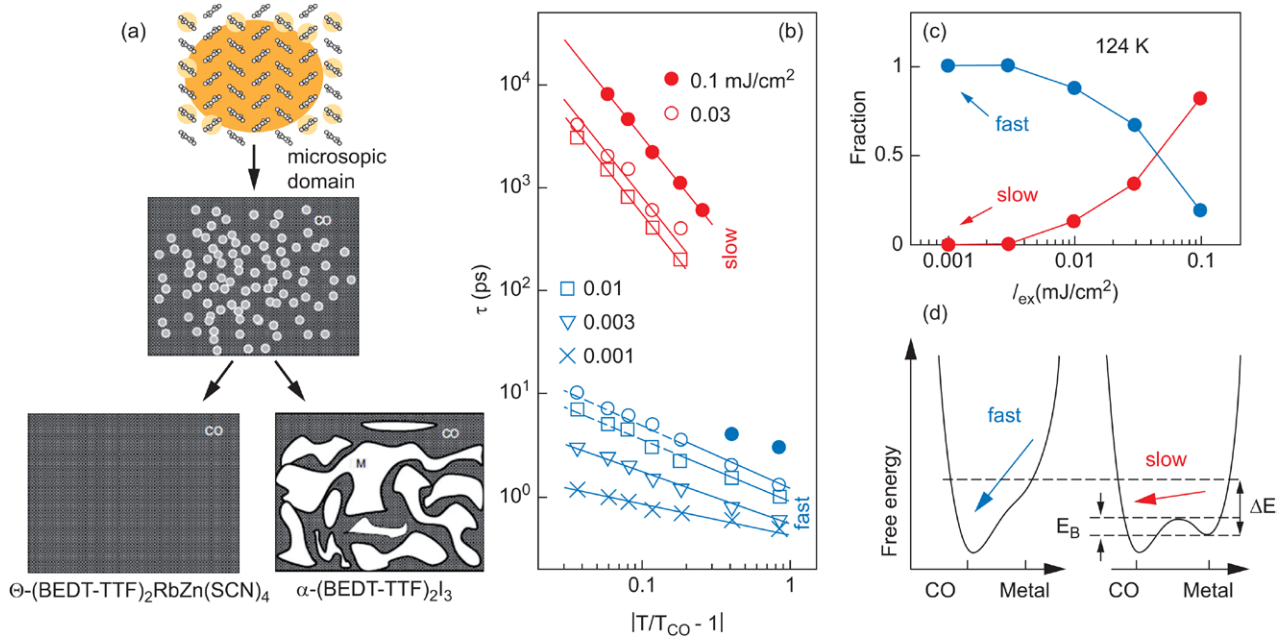


Figure 29. (a) Illustration how the microscopic metallic domains are produced initially; they can quickly recover the charge ordered state as in θ -(BEDT-TTF)₂RbZn(SCN)₄, or form macroscopic domains as in α -(BEDT-TTF)₂I₃ (after [154]). (b) Relaxation times of the photoinduced metallic state in α -(BEDT-TTF)₂I₃, τ_{fast} and τ_{slow} , as a function of reduced temperature $\frac{T_{CO} - T}{T_{CO}}$ for various excitation intensities I_{ex} at $T = 124$ K; (c) Fraction of the fast (blue dots: $\tau_{fast} \approx 1$ ps) and slow (red dots: $\tau_{slow} \approx 1$ ns) decay components are shown as a function of I_{ex} at $T = 124$ K; (d) Schematic illustrations of free energy surface for $T \ll T_{CO}$ (left: fast relaxation) and $T \approx T_{CO}$ (right: slow relaxation). The energy barrier E_B is much smaller than the thermal energy $k_B T \approx 10$ meV (after [155, 160]). Figure used with permission from Iwai (2012 *Crystals* 2 590). Copyright MDPI.

recently [174–176]; but at the moment, many open questions are still waiting to be answered. For this reason we give here only a brief account of the state of the art aiming to motivate further experimental and theoretical efforts in order to solve this interesting puzzle.

5.1. Ferroelectricity and magnetism

At high temperatures κ -(BEDT-TTF)₂Cu[N(CN)₂]Cl is an insulator with uniform charge distribution of one hole per BEDT-TTF dimer site. Optical spectroscopy reveals a crossover into the Mott insulator, which takes place below about 40 K [174, 177–179]. Accordingly, dc transport measurements indicate the presence of an insulator-to-insulator phase transition, but exact phase transition temperature and sharpness of the transition depend on the electric field orientation and vary among the single crystals measured [170, 174, 180]. Eventually, at lower temperatures, a weak ferromagnetic ground state (an antiferromagnetic state with canted spins) is established; the phase transition temperature, as in the charge sector, was found to be sample-dependent [181–185].

The nature of the phase transition in the charge-sector was proposed to be ferroelectric due to charge ordering in which BEDT-TTF dimer sites become non-equivalent [170]. In this scenario, the ordering of the electric dipoles on the BEDT-TTF dimers releases the spin frustration and results in the ferroelectricity-driven magnetic ordering. Experimental results supporting this picture include the Curie-like peak of the dielectric function (figure 32), the hysteresis and time-dependent

phenomena (figure 33) observed for electric fields applied perpendicular to molecular dimer planes at $T = 25$ K, that is in the vicinity of the magnetic phase transition [170, 182]. The absence of symmetry breaking, however, casts doubts on this proposal because it excludes static electric dipoles on the dimers. Vibrational spectroscopy puts an upper bound to the charge redistribution $\delta_p \approx \pm 0.005e$, thus seriously questioning the possibility that such a weak charge ordering, if any, constitutes the driving order parameter for magnetism. Importantly, the high-temperature side of ϵ' follows the Curie–Weiss behavior (section 2.2) and the extracted Curie constant results in the charge disproportionation, which is however 10 times larger than the upper bound given by optical measurements $2\delta_p \approx 0.01e$. The presence of extremely small dipoles $\pm\delta_p$ excludes any important ac-field-induced polarization within the sample volume. These facts point toward localized domain-wall motion as the excitations responsible for the observed Curie-like peak and the dielectric dispersion.

The presence of domain-wall motion on a disordered background is also indicated by an atypical shape of polarization-field hysteresis (figure 33) measured right at $T = 25$ K where the Curie-like peak of ϵ' was observed. The loop differs from the commonly observed loops in ferroelectrics [186] (see section 3.2) since it has a substantial linear part, which indicates that the dominant mechanism in this field range can only be some kind of continuous change such as the reversible rotation of the polarization within each domain toward the field direction. This paraelectric-like response implies the short-ranged nature of the domains whose size should be of the

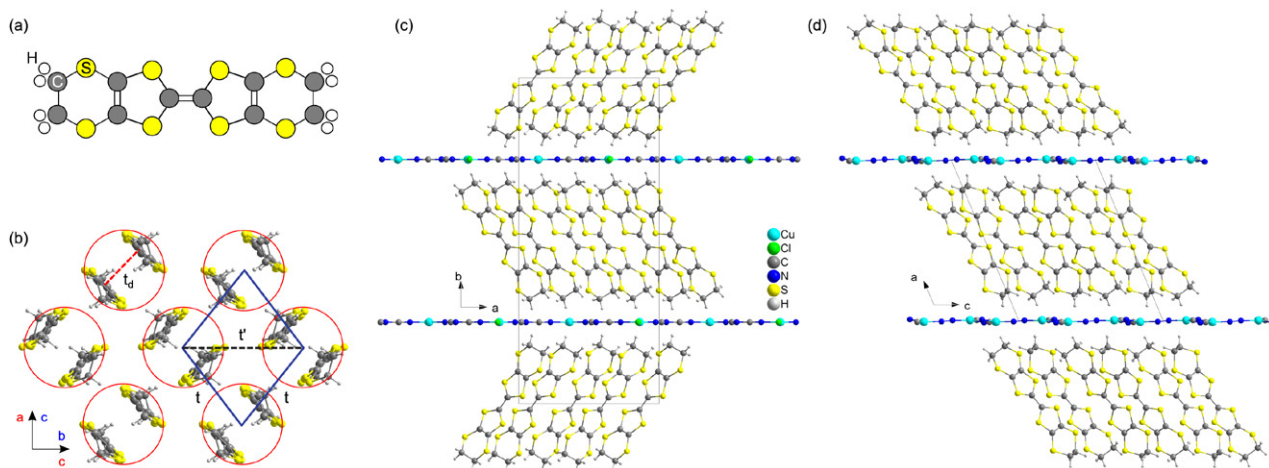


Figure 30. Crystallographic structure of κ -(BEDT-TTF) $_2$ Cu[N(CN) $_2$]Cl and κ -(BEDT-TTF) $_2$ Cu $_2$ (CN) $_3$. (a) Schematic drawing of a BEDT-TTF molecule, where BEDT-TTF stands for bis(ethylenedithio)tetrathiafulvalene; (b) View of BEDT-TTF dimers showing their triangular arrangement in the ((a), (c) and ((b), (c) plane. Side view of extended unit cell of κ -(BEDT-TTF) $_2$ Cu[N(CN) $_2$]Cl (c) and κ -(BEDT-TTF) $_2$ Cu $_2$ (CN) $_3$ (d) (after [166]).

order of the correlation length reflecting the strength of thermodynamic fluctuations in the vicinity of the phase transition. Nonlinearity at 5 Hz was observed only in a very restricted high-field range at $T = 25$ K, the upper bound was attributed to electric breakdown effects (see section 4.3). The fact that no nonlinear polarization-field hysteresis was observed at lower temperatures may indicate a very slow creep-like dynamics determined by relaxation of domain walls strongly pinned by disorder. A pinning potential could cause diverging barriers and lead to a nonlinear creep-like response for frequencies smaller than 0.01 Hz [187].

In order to reconcile these seemingly contradictory results, an alternative scenario was proposed recently [174] drawing the analogy to spin-density waves. For those the dielectric response was explained by invoking second-order harmonic charge modulation coupled with the magnetic order of itinerant spins in the presence of disorder [188–190]. In the case of κ -(BEDT-TTF) $_2$ Cu[N(CN) $_2$]Cl it was argued that the dielectric response can be explained by charged discommensurations of the commensurate antiferromagnetic phase in the temperature range above the magnetic phase transition, and charged domain-wall relaxations in the weak ferromagnetic state at lower temperatures. The overall charge and spin response in κ -(BEDT-TTF) $_2$ Cu[N(CN) $_2$]Cl indicates the presence of unconventional spin-charge coupling, as well as an important role of interaction with randomly distributed pinning centers. This may cause areas of fluctuating electronic dipoles on the dimers to couple to magnetic domains; domain walls between magnetic domains—in addition to spins—carry charge which accumulates within domain boundaries in order to promote the formation of magnetic order.

It might be worth to have a more detailed look at other κ -phase salts with an effectively half-filled band and which, nevertheless, exhibit charge-order phenomena. There are only a few compounds investigated so far, such as κ -(BEDT-TTF) $_4$ PtCl $_6$ ·C $_6$ H $_5$ CN, the triclinic κ -(BEDT-TTF) $_4$ [M(CN) $_6$][N(C $_2$ H $_5$) $_4$]·3H $_2$ O and the monoclinic κ -(BEDT-TTF) $_4$ [M(CN) $_6$]

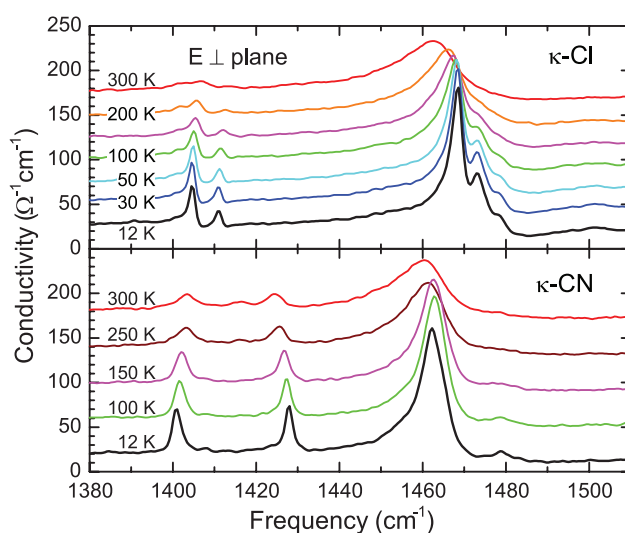


Figure 31. Temperature evolution of antisymmetric outer C=C double bond stretching mode $\nu_{27}(b_{1u})$ of BEDT-TTF molecule in κ -(BEDT-TTF) $_2$ Cu[N(CN) $_2$]Cl and κ -(BEDT-TTF) $_2$ Cu $_2$ (CN) $_3$. Its position at 1460 cm^{-1} corresponds to half a hole per molecule. No splitting indicating charge disproportionation occurs down to the lowest temperatures (after [166]).

[N(C $_2$ H $_5$) $_4$] $_2$ H $_2$ O (with $M = \text{Co}^{\text{III}}$, Fe^{III} , and Cr^{III}) salts [191–199] The structure is rather complex: the phase transition includes the deformation of the molecule and the coupling to the anions; accordingly details of their physical properties and their electronic states are not well-known. Certainly electronic correlations as well as coupling to the lattice are important. Recently, the system κ -(BEDT-TTF) $_2$ Hg(SCN) $_2$ Cl was shown to undergo a charge-order transition at 34 K; the metal insulator transition is linked to magnetic order [200, 201].

5.2. Ferroelectricity and quantum spin liquid

κ -(BEDT-TTF) $_2$ Cu $_2$ (CN) $_3$ is a Mott–Anderson dimer insulator with uniform charge distribution of one hole per BEDT-TTF dimer. DC transport happens via two-dimensional

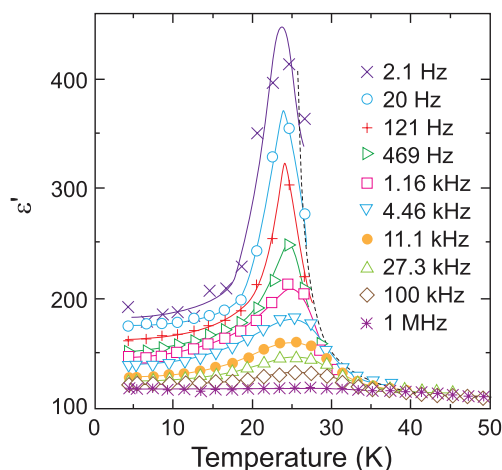


Figure 32. Peak of the real part of the dielectric function $\epsilon'(T)$ of κ -(BEDT-TTF)₂Cu[N(CN)₂]Cl measured with $\mathbf{E} \parallel \mathbf{b}$ for selected frequencies as a function of temperature (after [170]).

variable-range hopping among localized states and is attributed to the inherent disorder within the anion network [175, 202]. At low temperatures, a quantum spin liquid state is established; magnetic order is absent despite strong antiferromagnetic exchange coupling because an interplay of quantum effects and large frustration occurs on the triangular lattice [203]. The presence of low-lying spinon excitations is evidenced by the power-law behavior observed in the heat capacity, thermal conductivity and optical conductivity measurements [204, 205]. The overall charge, dielectric, spin and lattice response consistently show the presence of inhomogeneities, which grow gradually toward low temperatures and eventually acquire anomalous features in the vicinity of the phase transition at $T \approx 6$ K [168, 169, 172, 206–208]. Particularly based on lattice and dielectric data, it was suggested previously that the 6 K transition involves charges and that it may be associated with ferroelectric Curie and relaxor-like freezing of electric dipoles on BEDT-TTF dimers, predicted theoretically (figure 34) [168, 169]. This idea was abandoned because there exist neither data that indicate any symmetry breaking nor spectroscopic evidence for the static electric dipoles on the dimers. As a consequence, the following proposal was put forward [166]: there might exist fast temporal fluctuations of the charge distribution within the BEDT-TTF dimer of the order of 10^{11} Hz that are in accord with the rather broad vibrational lines, as plotted in figure 31. These fluctuating intradimer dipoles might be crucial for the microwave and terahertz response [171, 172, 209] since its softening was predicted theoretically [164]; however, they cannot be invoked to explain the dielectric response at low frequencies. Estimates based on the Curie–Weiss model (section 2.2) also discarded molecular dimer dipoles as the origin of the dielectric response since they yield values for the charge disproportionation 10–100 times larger than the upper bound put by vibrational data $2\delta_p \approx 0.01e$. Recent extensive dielectric measurements on single crystals with different levels of disorder suggested that the anomalous dielectric relaxation in κ -(BEDT-TTF)₂Cu₂(CN)₃ can be accounted for by charge defects

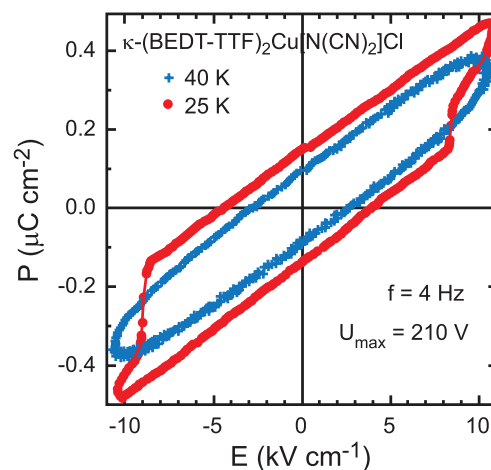


Figure 33. Polarization-electric field hysteresis curves at two representative temperatures 40 K (+, above the phase transition) and 25 K (●, in the vicinity of the phase transition) of κ -(BEDT-TTF)₂Cu[N(CN)₂]Cl measured at a frequency of 4 Hz with a maximum applied voltage of 210 V (after [170]).

generated in interfaces between frustration-limited domains whose creation is triggered by an inversion-symmetry breaking at a local scale in the anion network [175].

6. Comparative summary and outlook

In this review, the experimental aspects of electronic ferroelectricity and related electrostatics in the one-dimensional (TMTTF)₂X and TTF-CA, and in the most prominent phases of two-dimensional (BEDT-TTF)₂X molecular charge-transfer solids have been discussed and compared with predictions of current theoretical models. Despite the enormous research efforts devoted to this topic, it is by far not a closed chapter in the field of strongly correlated low-dimensional molecular solids.

By now it is well understood that electronic ferroelectricity is established in (TMTTF)₂X and TTF-CA, as well as in α -(BEDT-TTF)₂I₃ and the relaxed state of θ -(BEDT-TTF)₂RbZn(SCN)₄. Macroscopic electric polarization arises due to valence instability in TTF-CA and long-range charge order in the others; and is stabilized by a subtle interplay of Coulomb forces and structural changes. The charge disproportionation was evidenced by a variety of experimental techniques including NMR, x-ray and neutron diffraction, Raman and infrared vibrational spectroscopy and optical second harmonic generation; they probe the local order as well as the global symmetry.

Remarkably, even when non-equivalent bonds are already present in the native structure, additional structural changes set in and enhance the breaking the inversion symmetry. Type and magnitude of changes differ for these compounds ranging from dimerization in TTF-CA and changes of dihedral angles in α -(BEDT-TTF)₂I₃, changes of dihedral angles accompanied by doubling of the unit cell in θ -(BEDT-TTF)₂RbZn(SCN)₄ to an uniform anion shift as a whole in the (TMTTF) salts. The role

of cation-anion hydrogen bond interactions have been also suggested for $(\text{TMTTF})_2\text{X}$ and $\alpha\text{-(BEDT-TTF)}_2\text{I}_3$. Taken together experimental data and current theoretical approaches, there are clear indications that the stabilization of electronic ferroelectricity takes place by a cooperative process between Coulomb interactions and coupled molecular cation-anion subsystems.

The electrodynamic properties demonstrating the ferroelectric nature of the charge-ordered state include: a Curie-like peak of the dielectric constant and its characteristic dispersion, strong non-linear effects, switching, polarization hysteresis and ultra-fast dynamics. Polarization hysteresis, commonly taken as a basic piece of evidence for ferroelectricity has only been observed in TTF-CA. The missing evidence in the other systems may be due to either relatively high conductivity or to a low breakdown field; certainly more efforts are needed to clarify this issue.

Optical nonlinearity and ultra-fast photo-response observed in TTF-CA, and in $\alpha\text{-(BEDT-TTF)}_2\text{I}_3$ and $\theta\text{-(BEDT-TTF)}_2\text{RbZn(SCN)}_4$ strongly support an intrinsic electronic origin of the ferroelectricity. Effects include the light-induced melting of the charge-ordered state and creation of metallic domains within extremely short times at the level of pico- to femtoseconds and decay back to the original state. A quantitative difference observed in photo-induced dynamics among these systems can be correlated with different structural changes involved in the formation of the ferroelectric state. On the other hand, dc electric field-induced effects such as negative differential resistance and switching happen within much longer, i.e. millisecond time scales and thus can hardly be explained by melting. One of the plausible mechanisms involves the domain wall dynamics; this issue remains to be explored further. The formation of ferroelectric domains was visualized by electro-reflectance and optical second harmonic generation interferometry in TTF-CA and $\alpha\text{-(BEDT-TTF)}_2\text{I}_3$; their presence was invoked in interpretation of the dielectric response at lower temperatures, away from the charge-ordering phase transition in $(\text{TMTTF})_2\text{X}$, TTF-CA and $\alpha\text{-(BEDT-TTF)}_2\text{I}_3$.

The dielectric response features a Curie peak with negligible dispersion at the charge ordering and neutral-to-ionic phase transition temperature and a characteristic response at lower temperatures. Pre-transitional effects are also observed in $\alpha\text{-(BEDT-TTF)}_2\text{I}_3$ and relaxed state of $\theta\text{-(BEDT-TTF)}_2\text{RbZn(SCN)}_4$ up to room temperatures. Anomalous features of the dielectric response indicate the critical role of random potential arising due to internal heterogeneity. It may influence the scale at which charge order develops thus, for example, affecting the formation of a Curie peak at the phase transition, and even resulting in relaxor ferroelectricity in nominally pure single crystals, as observed for $(\text{TMTTF})_2\text{X}$ and TTF-CA. Importantly, for the best single crystals, estimates of charge disproportionation deduced from the Curie constant strongly deviate from well established values for $(\text{TMTTF})_2\text{X}$ and TTF-CA, while they are close to them for $\alpha\text{-(BEDT-TTF)}_2\text{I}_3$ and $\theta\text{-(BEDT-TTF)}_2\text{RbZn(SCN)}_4$. These findings are intriguing and call for further considerations.

Finally, we have taken a look at the electrodynamic properties of two most challenging materials

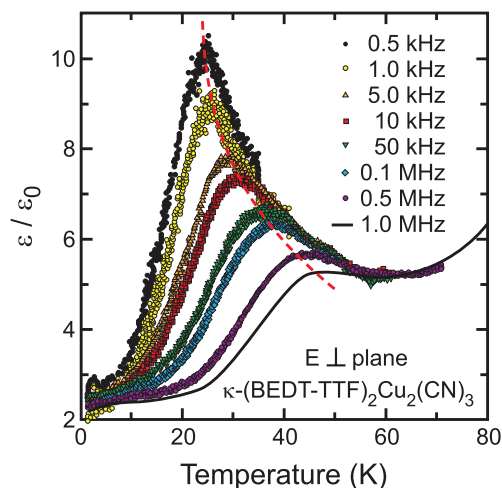


Figure 34. Relaxor-like peak of the real part of the dielectric function ϵ' for selected frequencies and $\mathbf{E} \parallel a$ of $\kappa\text{-(BEDT-TTF)}_2\text{Cu}_2(\text{CN})_3$ (after [169]).

$\kappa\text{-(BEDT-TTF)}_2\text{Cu}[\text{N}(\text{CN})_2]\text{Cl}$ and $\kappa\text{-(BEDT-TTF)}_2\text{Cu}_2(\text{CN})_3$ suggested as candidates for a molecular multiferroic and quantum spin liquid, respectively. These systems display an anomalous dielectric response in the absence of structural changes and with no evidence for charge disproportionation. A polarization hysteresis and bistable resistance are also reported for $\kappa\text{-(BEDT-TTF)}_2\text{Cu}[\text{N}(\text{CN})_2]\text{Cl}$. Advanced experimental probes and theoretical approaches are required to achieve a very much needed breakthrough in understanding of these phenomena.

Future research in the field of low-dimensional molecular solids, experimental as well as theoretical, should focus on the search of novel candidates for ferroelectricity and multiferroicity due to their growing importance in fundamental as well as applied research areas. Evidently, different aspects of their unique correlated electron dynamics, in particular an ultra-fast photo-response may find application in ultra-fast switching devices.

Acknowledgments

We thank I Balog, M Basletić, N Drichko, A Girlando, T Ivek, B Korin-Hamzić, O Milat, T Peterseim, M Pinterić, and E Rose for the fruitful collaborations. We also acknowledge stimulating discussions with S. Brazovskii, S Brown, S Ishihara, K Kanoda, M Lang, P Monceau and J-P Pouget. The project was supported by the Deutsche Forschungsgemeinschaft (DFG), the Deutsche Akademische Auslandsdienst (DAAD) and by the Croatian Science Foundation project IP-2013-11-1011.

References

- [1] Dagotto E 2001 *Phys. Rep.* **344** 1
- [2] Seo H 2000 *J. Phys. Soc. Japan* **69** 805
- [3] Yoshioka H, Otsuka Y and Seo H 2012 *Crystals* **2** 996
- [4] Hotta C 2012 *Crystals* **2** 1155
- [5] Ikeda N *et al* 2005 *Nature* **436** 1136

- [6] Hemberger J 2005 *Nature* **434** 364
- [7] Milward G C, Calderon M J and Littlewood P B 2005 *Nature* **433** 607
- [8] Kimura T, Seiko Y, Nakamura H, Siegrist T and Ramirez A P 2008 *Nat. Mater.* **7** 291
- [9] Portengen T, Östreich Th and Sham L J 1996 *Phys. Rev. B* **54** 17452
- [10] Efremov D V, Van den Brink J and Khomskii D I 2004 *Nat. Mater.* **3** 853
- [11] Van den Brink J and Khomskii D I 2008 *J. Phys.: Condens. Matter* **20** 434217
- [12] Cross L E 1987 *Ferroelectrics* **76** 241
- [13] Vugmeister B E and Glinchuk M D 1990 *Rev. Mod. Phys.* **62** 993
- [14] Wright J P, Attfield J P and Radaelli P G 2002 *Phys. Rev. B* **66** 214422
- [15] Spaldin N A and Fiebig M 2005 *Science* **309** 391
- [16] Ishihara S 2010 *J. Phys. Soc. Japan* **79** 011010
- [17] Grüner G 1988 *Rev. Mod. Phys.* **60** 1129
- [18] Uchino K 2000 *Ferroelectric Devices* (New York: Marcel Dekker)
- [19] Rabe K M, Ahn C H and Triscone J-M (ed) 2007 *Physics of Ferroelectrics: a Modern Perspective* (Topics in Applied Physics vol 105) (Berlin: Springer)
- [20] Horiuchi S and Tokura Y 2008 *Nat. Mater.* **7** 357
- [21] Brazovskii S A 2008 Ferroelectricity and charge ordering in quasi-1D organic conductors *The Physics of Organic Superconductors and Conductors* ed A Lebed (Berlin: Springer) pp 313–55
- [22] Monceau P 2012 *Adv. Phys.* **61** 325
- [23] Horiuchi S 2006 *Chem. Phys.* **325** 78
- [24] Horiuchi S, Hasegawa T and Tokura Y 2006 *J. Phys. Soc. Japan* **75** 051016
- [25] Chow D S, Zamborszky F, Alavi B, Tantillo D J, Baur A, Merlic C A and Brown S E 2000 *Phys. Rev. Lett.* **85** 1698
- [26] Takahashi T, Nogami Y and Yakushi K 2006 *J. Phys. Soc. Japan* **75** 051008
- [27] Matsunaga N, Hirose S, Shimohara N, Satoh T, Isome T, Yamamoto M, Liu Y, Kawamoto A and Nomura K 2013 *Phys. Rev. B* **87** 144415
- [28] Dumm M, Salameh B, Abaker M, Montgomery L K and Dressel M 2004 *J. Phys. IV France* **114** 57
- [29] Dressel M, Dumm M, Knoblauch T and Masino M 2012 *Crystals* **2** 528
- [30] Dressel M and Drichko N 2004 *Chem. Rev.* **104** 5689
- [31] Knoblauch T and Dressel M 2012 *Phys. Status Solidi* **9** 1158
- [32] Meneghetti M, Bozio R, Zanon I, Pecile C, Ricotta C and Zanetti M 1984 *J. Chem. Phys.* **80** 6210
- [33] Seo H and Fukuyama H 1997 *J. Phys. Soc. Japan* **66** 1249
- [34] Foury-Leylekian P, Petit S, Andre G, Moradpour A and Pouget J-P 2010 *Physica B* **405** S95
- [35] De Souza M, Foury-Leylekian P, Moradpour A, Pouget J-P and Lang M 2008 *Phys. Rev. Lett.* **101** 216403
- [36] De Souza M, Hofmann D, Foury-Leylekian P, Moradpour A, Pouget J-P and Lang M 2008 *Physica B* **405** S92
- [37] Pouget J-P, Foury-Leylekian P, Alemany P and Canadell E 2012 *Phys. Status Solidi B* **249** 937
- [38] De Souza M and Pouget J-P 2013 *J. Phys.: Condens. Matter* **25** 343201
- [39] Rose E and Dressel M 2012 *Physica B* **407** 1787
- [40] Riera J and Poilblanc D 2001 *Phys. Rev. B* **63** 241102
- [41] Yasin S, Salameh B, Rose E, Dumm M, Krug von Nidda H-A, Loidl A, Ozerov M, Untereiner G, Montgomery L K and Dressel M 2012 *Phys. Rev. B* **85** 144428
- [42] Dressel M, Dumm M, Knoblauch T, Köhler B, Salameh B and Yasin S 2012 *Adv. Condens. Matter Phys.* **2012** 398721
- [43] Moncesu P, Nad F Ya and Brazovskii S 2001 *Phys. Rev. Lett.* **86** 4080
- [44] Nad F, Monceau P, Kaboub L and Fabre J M 2006 *Europhys. Lett.* **73** 567
- [45] Starešinić D, Biljaković K, Lunkenheimer P and Loidl A 2006 *Solid State Commun.* **137** 241
- [46] Nad F and Monceau P 2006 *J. Phys. Soc. Japan* **75** 051005
- [47] Lines M and Glass A 1979 *Principles and Applications of Ferroelectrics and Related Materials* (Oxford: Clarendon)
- [48] Brazovskii S, Monceau P and Nad F Ya 2015 *Physica B* **460** 79
- [49] Langlois A, Poirier M, Bourbonnais C, Foury-Leylekian P, Moradpour A and Pouget J-P 2010 *Phys. Rev. B* **81** 125101
- [50] Nad F, Monceau P, Carcel C and Fabre J M 2000 *Phys. Rev. B* **62** 1753
- [51] Kagoshima S, Kanai Y, Tani M, Tokura Y and Koda T 1985 *Mol. Cryst. Liq. Cryst.* **120** 9
- [52] Le Cointe M, Lemée-Cailleau M H, Cailleau H, Toudic B, Toupet L, Heger G, Moussa F, Schweiss P, Kraft K H and Karl N 1995 *Phys. Rev. B* **51** 3374
- [53] Horiuchi S, Kumai R, Okimoto Y and Tokura Y 2006 *Chem. Phys.* **325** 78
- [54] Batail P, LaPlaca S J, Mayerle J J and Torrance J B 1981 *J. Am. Chem. Soc.* **103** 951
- [55] Torrance J B, Vazquez J E, Mayerle J J and Lee V Y 1981 *Phys. Rev. Lett.* **46** 253
- [56] Girlando A, Marzola F, Pecile C and Torrance J B 1983 *J. Chem. Phys.* **79** 1075
- [57] Mayerle J J, Torrance J B and Crowley J I 1979 *Acta Crystallogr. B* **35** 2988
- [58] Girlando A, Bozio R, Pecile C and Torrance J B 1982 *Phys. Rev. B* **26** 2306
- [59] Rice M J, Lipari N O and Strässler S 1977 *Phys. Rev. Lett.* **39** 1359
- [60] Dengl A, Beyer R, Peterseim T, Ivek T, Untereiner G and Dressel M 2014 *J. Chem. Phys.* **140** 244511
- [61] Masino M, Girlando A and Soos Z G 2003 *Chem. Phys. Lett.* **369** 428
- [62] Tokura Y, Koda T, Mitani T and Saito G 1982 *Solid State Commun.* **43** 757
- [63] Kikuchi K, Yakushi K and Kuroda H 1982 *Solid State Commun.* **44** 151
- [64] Jacobsen C S and Torrance J B 1983 *J. Chem. Phys.* **78** 112
- [65] Horiuchi S, Okimoto Y, Kumai R and Tokura Y 2000 *J. Phys. Soc. Japan* **69** 1302
- [66] Horiuchi S, Kumai R, Okimoto Y and Tokura Y 2000 *Phys. Rev. Lett.* **85** 5210
- [67] Peterseim T, Haremski P and Dressel M 2015 *Europhys. Lett.* **109** 67003
- [68] Gourdji M, Guibé L, Péneau A, Gallier J, Toudic B and Cailleau H 1991 *Solid State Commun.* **77** 609
- [69] Gourdji M, Guibé L, Péneau A, Gallier J, Toudic B and Cailleau H 1992 *Z. Naturforsch.* **47a** 257
- [70] LeCointe M, Gallier J, Cailleau H, Gourdji M, Péneau A and Guibé L 1995 *Solid State Commun.* **94** 455
- [71] Girlando A, Pecile C and Torrance J 1985 *Solid State Commun.* **54** 753
- [72] Avignon M, Balseiro C A, Proetto C R and Alascio B 1986 *Phys. Rev. B* **33** 205
- [73] Girlando A and Painelli A 1986 *Phys. Rev. B* **34** 2131
- [74] Nagaosa N 1986 *J. Phys. Soc. Japan* **55** 2754
- [75] Masino M, Girlando A, Brillante A, Valle R D, Venuti E, Drichko N and Dressel M 2006 *Chem. Phys.* **325** 71
- [76] Girlando A, Masino M, Painelli A, Drichko N, Dressel M, Brillante A, Della Valle R G and Venuti E 2008 *Phys. Rev. B* **78** 045103
- [77] Moreac A, Girard A, Delugeard Y and Marqueton Y 1996 *J. Phys.: Condens. Matter* **8** 3553
- [78] Girlando A, Painelli A, Bewick S and Soos Z 2004 *Synth. Met.* **141** 129

- [79] Okimoto Y, Horiuchi S, Saitoh E, Kumai R and Tokura Y 2001 *Phys. Rev. Lett.* **87** 187401
- [80] Soos Z G, Bewick S A, Peri A and Painelli A 2004 *J. Chem. Phys.* **120** 6712
- [81] Tokura Y, Koshihara S, Iwasa Y, Okamoto H, Komatsu T, Koda T, Iwasawa N and Saito G 1989 *Phys. Rev. Lett.* **63** 2405
- [82] Okamoto H, Mitani T, Tokura Y, Koshihara S, Komatsu T, Iwasa Y, Koda T and Saito G 1991 *Phys. Rev. B* **43** 8224
- [83] Kobayashi K, Horiuchi S, Kumai R, Kagawa F, Murakami Y and Tokura Y 2012 *Phys. Rev. Lett.* **108** 237601
- [84] Horiuchi S, Kumai R and Tokura Y 1998 *J. Am. Chem. Soc.* **120** 7379
- [85] Horiuchi S, Kumai R, Okimoto Y and Tokura Y 1999 *Phys. Rev. B* **59** 11267
- [86] Horiuchi S, Okimoto Y, Kumai R and Tokura Y 2001 *J. Am. Chem. Soc.* **123** 665
- [87] Horiuchi S, Okimoto Y, Kumai R and Tokura Y 2003 *Science* **299** 229
- [88] Tokura Y, Kaneko Y, Okamoto H, Tanuma S, Koda T, Mitani T and Saito G 1985 *Mol. Cryst. Liq. Cryst.* **125** 71
- [89] Kishida H, Takamatsu H, Fujinuma K and Okamoto H 2009 *Phys. Rev. B* **80** 205201
- [90] Tokura Y, Okamoto H, Koda T, Mitani T and Saito G 1988 *Phys. Rev. B* **38** 2215
- [91] Kagawa F, Horiuchi S, Matsui H, Kumai R, Onose Y, Hasegawa T and Tokura Y 2010 *Phys. Rev. Lett.* **104** 227602
- [92] Painelli A and Girlando A 1987 *J. Chem. Phys.* **67** 1705
- [93] Del Freo L, Painelli A and Seos Z G 2002 *Phys. Rev. Lett.* **89** 027402
- [94] Nagahori A, Kubota K and Itoh C 2013 *Eur. Phys. J. B* **86** 09
- [95] Collet E, Buron-Le Cointe M and Cailleau H 2006 *J. Phys. Soc. Japan* **75** 011002
- [96] Yonemitsu K 2012 *Crystals* **2** 56
- [97] Nasu K 2004 *Photoinduced Phase Transition* (Singapore: World Scientific)
- [98] Tokura Y 2006 *J. Phys. Soc. Japan* **75** 011001
- [99] Koshihara, S-Y, Tokura Y, Mitani T, Saito G and Koda T 1990 *Phys. Rev. B* **42** 6853
- [100] Koshihara, S-Y, Takahashi Y, Sakai H, Tokura Y and Luty T 1999 *J. Phys. Chem. B* **103** 2592
- [101] Huai P, Zheng H and Nasu K 2000 *J. Phys. Soc. Japan* **69** 1788
- [102] Iwai S, Tanaka S, Fujinuma K, Kishida H, Okamoto H and Tokura Y 2002 *Phys. Rev. Lett.* **88** 057402
- [103] Tanimura K 2004 *Phys. Rev. B* **70** 144112
- [104] Okamoto H, Ishige Y, Tanaka S, Kishida H, Iwai S and Tokura Y 2004 *Phys. Rev. B* **70** 165202
- [105] Collet E, Lemée-Cailleau M H, Buron-Le Cointe M, Cailleau H, Ravy S, Luty T, Bérar J F, Czarnecki P and Karl N 2002 *Europhys. Lett.* **57** 67
- [106] Luty T *et al* 2002 *Europhys. Lett.* **59** 619
- [107] Guérin L, Collet E, Leme-Cailleau M H, Buron-Le Cointe M, Cailleau H, Plech A, Wulff M, Koshihara S-Y and Luty T 2004 *Chem. Phys.* **299** 163
- [108] Collet E, Lorenc M, Cailleau H and Buron-Le Cointe M 2013 *Comprehensive Inorganic Chemistry II* 2nd edn ed J Reedijk and K Poepelmeier (Amsterdam: Elsevier) p 161
- [109] Matsubara Y, Yoshida T, Ishikawa T, Okimoto Y, Koshihara S-Y and Onda K 2012 *Acta Phys. Pol. A* **121** 340
- [110] Tanimura K and Akimoto I 2001 *J. Lumin.* **94-5** 483
- [111] Yonemitsu K 2011 *J. Phys. Soc. Japan* **80** 084707
- [112] Uemura H and Okamoto H 2010 *Phys. Rev. Lett.* **105** 258302
- [113] Miyamoto T, Uemura H and Okamoto H 2012 *J. Phys. Soc. Japan* **81** 073703
- [114] Bender K, Hennig I, Schweitzer D, Dietz K, Endres H and Keller H J 1984 *Mol. Cryst. Liq. Cryst.* **108** 359
- [115] Mori T, Kobayashi A, Sasaki Y, Kobayashi H, Saito G and Inokuchi H 1984 *Chem. Lett.* **1984** 957
- [116] Bender K, Dietz K, Endres H, Helberg W, Hennig I, Keller H J, Schäfer H W and Schweitzer D 1984 *Mol. Cryst. Liq. Cryst.* **107** 45
- [117] Alemany P, Pouget J-P and Canadell E 2012 *Phys. Rev. B* **85** 195118
- [118] Mori T 1998 *Bull. Chem. Soc. Japan* **71** 2509
Mori T 1999 *Bull. Chem. Soc. Japan* **72** 179
Mori T, Mori H and Tanaka S 1999 *Bull. Chem. Soc. Japan* **72** 2011
- [119] Mori H, Tanaka S, Mori T 1998 *Phys. Rev. B* **57** 12023
- [120] Kakiuchi T, Wakabayashi Y, Sawa H, Takahashi T and Nakamura T 2007 *J. Phys. Soc. Japan* **76** 113702
- [121] Guionneau P, Kepert C J, Bravic G, Chasseau D, Truter M R, Kurmoo M and Day P 1997 *Synth. Met.* **86** 1973
- [122] Ivek T, Korin-Hamzić B, Milat O, Tomić S, Clauss C, Drichko N, Schweitzer D and Dressel M 2011 *Phys. Rev. B* **83** 165128
- [123] Rothaemel B, Forro L, Cooper J R, Schilling J S, Weger M, Bele P, Brunner H, Schweitzer D and Keller H J 1986 *Phys. Rev. B* **34** 704
- [124] Yamamoto K, Kowalska A A and Yakushi K 2010 *Appl. Phys. Lett.* **96** 122901
- [125] Takano Y, Hiraki K, Yamamoto H M, Nakamura T and Takahashi T 2001 *J. Phys. Chem. Solids* **62** 393
- [126] Moldenhauer J, Horn C, Pokhodnia K I, Schweitzer D, Heinen I and Keller H J 1993 *Synth. Met.* **60** 31
- [127] Wojciechowski R, Yamamoto K, Yakushi K, Inokuchi M and Kawamoto A 2003 *Phys. Rev. B* **67** 224105
- [128] Yue Y, Yamamoto K, Uruichi M, Nakano C, Yakushi K, Yamada S, Hiejima T and Kawamoto A 2010 *Phys. Rev. B* **82** 075134
- [129] Clauss C, Drichko N, Schweitzer D and Dressel M 2010 *Physica B* **405** S144
- [130] Hirata M, Ishikawa K, Miyagawa K, Kanoda K and Tamura M 2011 *Phys. Rev. B* **84** 125133
- [131] Yamamoto T, Uruichi M, Yamamoto K, Yakushi K, Kawamoto A and Taniguchi H 2005 *J. Phys. Chem. B* **109** 15226
- [132] Seo H, Merino J, Yoshioka H and Ogata M 2006 *J. Phys. Soc. Japan* **75** 051009
- [133] Yamamoto K, Iwai S, Boyko S, Kashiwazaki A, Hiramatsu F, Okabe C, Nishi N and Yakushi K 2008 *J. Phys. Soc. Japan* **77** 074709
- [134] Chiba R, Hiraki K, Sakurai Y, Takahashi T, Yamamoto H M and Nakamura T 2004 *Phys. Rev. Lett.* **93** 216405
- [135] Watanabe M, Noda Y, Nogami Y and Mori H 2004 *J. Phys. Soc. Japan* **73** 116
- [136] Mori H, Tanaka S, Mori T, Kobayashi A and Kobayashi H 1998 *Bull. Chem. Soc. Japan* **71** 797
- [137] Miyagawa K, Kawamoto A and Kanoda K 2000 *Phys. Rev. B* **62** R7679
- [138] Chiba R, Yamamoto H, Hiraki K, Takahashi T and Nakamura T 2001 *J. Phys. Chem. Solids* **62** 389
- [139] Wang N L, Mori H, Tanaka S, Dong J and Clayman B P 2001 *J. Phys.: Condens. Matter* **13** 5463
- [140] Yamamoto K, Yakushi K, Miyagawa K, Kanoda K and Kawamoto A 2002 *Phys. Rev. B* **65** 085110
- [141] Drichko N, Kaiser S, Sun Y, Clauss C, Dressel M, Mori H, Schlueter J, Zhyliaeva E I, Torunova S A and Lyubovskaya R N 2009 *Physica B* **404** 490
- [142] Yakushi K 2012 *Crystals* **2** 1291
- [143] Clay R T, Mazumdar S and Campbell D K 2002 *J. Phys. Soc. Japan* **71** 1816
- [144] Dressel M, Grüner G, Pouget J P, Breining A and Schweitzer D 1994 *J. Phys. I France* **4** 579

- [145] Ivek T, Korin-Hamzić B, Milat O, Tomić S, Clauss C, Drichko N, Schweitzer D and Dressel M 2010 *Phys. Rev. Lett.* **104** 206406
- [146] Kodama K, Kimata M, Takahide Y, Kurita N, Harada A, Satsukawa H, Terashima T, Uji S, Yamamoto K and Yakushi K 2012 *J. Phys. Soc. Japan* **81** 044703
- [147] Lunkenheimer P, Hartmann B, Lang M, Mueller J, Schweitzer D, Krohns S and Loidl A 2015 *Phys. Rev. B* **91** 245132
- [148] Monceau P 2014 private communication
- [149] Moncesu P, Nad F and Yamamoto H M 2006 *J. Phys.: Condens. Matter* **18** L509
- [150] Inagaki K, Terasaki I and Mori H 2003 *Physica B* **329** 1162
- [151] Ivek T, Kovacević I, Pinterić M, Korin-Hamzić B, Tomić S, Knoblauch T, Schweitzer D and Dressel M 2012 *Phys. Rev. B* **86** 245125
- [152] Iwai S, Yamamoto K, Kashiwazaki A, Hiramatsu F, Nakaya H, Kawakami Y, Yakushi K, Okamoto H, Mori H and Nishio Y 2007 *Phys. Rev. Lett.* **98** 097402
- [153] Kawakami Y, Fukatsu T, Sakurai Y, Unno H, Itoh H, Iwai S, Sasaki T, Yamamoto K, Yakushi K and Yonemitsu K 2010 *Phys. Rev. Lett.* **105** 246402
- [154] Iwai S 2011 *J. Lumin.* **131** 409
- [155] Iwai S 2012 *Crystals* **2** 590
- [156] Miyashita S, Tanaka Y, Iwai S and Yonemitsu K 2010 *J. Phys. Soc. Japan* **79** 034708
- [157] Tanaka Y and Yonemitsu K 2010 *J. Phys. Soc. Japan* **79** 024712
- [158] Tanaka Y and Yonemitsu K 2008 *J. Phys. Soc. Japan* **77** 034708
- [159] Miyashita S and Yonemitsu K 2007 *Phys. Rev. B* **75** 245112
- [160] Iimori T, Naito T and Ohta N 2007 *Chem. Lett.* **36** 536
- [161] Tamura K, Ozawa T, Bando Y, Kawamoto T and Mori T 2010 *J. Appl. Phys.* **107** 103716
- [162] Dressel M, Grüner, Pouget J P, Breining A and Schweitzer D 1995 *Synth. Met.* **70** 929
- [163] Hotta C 2010 *Phys. Rev. B* **82** 241104
- [164] Naka M and Ishihara S 2010 *J. Phys. Soc. Japan* **79** 063707
Naka M and Ishihara S 2013 *J. Phys. Soc. Japan* **82** 023701
- [165] Li H, Clay R T and Mazumdar S 2010 *J. Phys.: Condens. Matter* **22** 272201
Dayal S, Clay R T, Li H and Mazumdar S 2011 *Phys. Rev. B* **83** 245106
- [166] Sedlmeier K, Elsässer S, Neubauer D, Beyer R, Wu D, Ivek T, Tomić S, Schlueter J A and Dressel M 2012 *Phys. Rev. B* **86** 245103
- [167] Kanoda K 2012 private communication
- [168] Manna R S, de Souza M, Brühl A, Schlueter J A and Lang M 2010 *Phys. Rev. Lett.* **104** 016403
- [169] Abdel-Jawad M, Terasaki I, Sasaki T, Yoneyama N, Kobayashi N, Uesu Y and Hotta C 2010 *Phys. Rev. B* **82** 125119
- [170] Lunkenheimer P *et al* 2012 *Nat. Mater.* **11** 755
- [171] Poirier M, Parent S, Côté A, Miyagawa K, Kanoda K and Shimizu Y 2012 *Phys. Rev. B* **85** 134444
- [172] Itoh K, Itoh H, Naka M, Saito S, Hosako I, Yoneyama N, Ishihara S, Sasaki T and Iwai S 2013 *Phys. Rev. Lett.* **110** 106401
- [173] Lang M, Lunkenheimer P, Müller J, Loidl A, Hartmann B, Hoang N H, Gati E, Schubert H and Schlueter J A 2014 *IEEE Trans. Magn.* **50** 2700107
- [174] Tomić S, Pinterić M, Ivek T, Sedlmeier K, Beyer R, Wu D, Schlueter J A, Schweitzer D and Dressel M 2013 *J. Phys.: Condens. Matter* **25** 436004
- [175] Pinterić M *et al* 2014 *Phys. Rev. B* **90** 195139
- [176] Pinterić M, Ivek T, Čulo M, Milat O, Basletić M, Korin-Hamzić B, Tafra E, Hamzić A, Dressel M and Tomić S 2015 *Physica B* **460** 202
- [177] Kornelsen K, Eldridge J E, Wang H H, Charlier H A and Williams J M 1992 *Solid State Commun.* **81** 343
- [178] Faltermeier D, Barz J, Dumm M, Dressel M, Drichko N, Petrov B, Semkin V, Vlasova R, Mézière C and Batail P 2007 *Phys. Rev. B* **76** 165113
Dumm M, Faltermeier D, Drichko N, Dressel M, Mézière C and Batail P 2009 *Phys. Rev. B* **79** 195106
- [179] Elsässer S, Wu D, Dressel M and Schlueter J A 2012 *Phys. Rev. B* **86** 155150
- [180] Williams J M *et al* 1990 *Inorg. Chem.* **29** 3272
- [181] Welp U, Fleshler S, Kwok W K, Crabtree G W, Carlson K D, Wang H H, Geiser U, Williams J M and Hitsman V M 1992 *Phys. Rev. Lett.* **69** 840
- [182] Kawamoto A, Miyagawa K, Nakazawa Y and Kanoda K 1995 *Phys. Rev. B* **52** 15522
- [183] Kubota M, Saito G, Ito H, Ishiguro T and Kojima N 1996 *Mol. Liq. Liq. Cryst.* **284** 367
- [184] Pinterić M, Miljak M, Biškup N, Milat O, Aviani I, Tomić S, Schweitzer D, Strunz W and Heinen I 1999 *Eur. Phys. J. B* **11** 217
- [185] Smith D F, De Soto S M and Slichter C P 2003 *Phys. Rev. B* **68** 024512
- [186] Kagawa F, Horiuchi S, Tokunaga M, Fujioka J and Tokura Y 2010 *Nat. Phys.* **6** 169
- [187] Kleemann W 2010 *Annu. Rev. Mater. Res.* **37** 415
- [188] Tomić S, Cooper J R, Jerome D and Bechgaard K 1989 *Phys. Rev. Lett.* **62** 462
- [189] Zornoza P, Petkhov K, Dressel M, Biškup N, Vuletić T and Tomić S 2005 *Eur. Phys. J. B* **46** 223
- [190] Maki K and Virosztek A 1989 *Phys. Rev. B* **39** 9640
- [191] Doublet M-L, Canadell E and Shibaeva R P 1994 *J. Phys. I France* **4** 1479
- [192] Le Maguerès P, Ouahab L, Conan N, Gomez-García C J, Delhaës P, Even J and Bertault M 1996 *Solid State Commun.* **97** 27
- [193] Ouahab L, Golhen S, Le Hoerff T, Guillevic J, Tual L, Hélou N, Amiel J, Delhaës P, Binet K and Fabre J M 1999 *Synth. Met.* **102** 1642
- [194] Świetlik R, Łapiński A, Ouahab L and Yakushi K 2003 *C. R. Chim.* **6** 395
- [195] Świetlik R, Łapiński A, Polomska M, Ouahab L and Guillevic J 2003 *Synth. Met.* **133** 273
- [196] Świetlik R, Ouahab L, Guillevic J and Yakushi K 2004 *Macromol. Symp.* **212** 219
- [197] Świetlik R, Łapiński A, Polomska M, Ouahab L and Ota A 2006 *J. Low Temp. Phys.* **142** 641
- [198] Ota A, Ouahab L, Golhen S, Yoshida Y, Maestro M, Saito G and Świetlik R 2007 *Chem. Mater.* **19** 2455
- [199] Łapiński A, Świetlik R, Ouahab L and Golhen S 2013 *J. Phys. Chem. A* **117** 5241
- [200] Yasin S, Rose E, Dumm M, Drichko N, Dressel M, Schlueter J A, Zhilyaeva E I, Torunova S and Lyubovskaya R N 2012 *Physica B* **407** 1689
- [201] Drichko N, Beyer R, Yasin S, Dressel M, Schlueter J A, Zhilyaeva E I, Torunova S and Lyubovskaya R N 2014 *Phys. Rev. B* **89** 075133
- [202] Čulo M, Tafra E, Basletić M, Tomić S, Hamzić A, Korin-Hamzić B, Dressel M, Schlueter J A 2015 *Physica B* **460** 208
- [203] Shimizu Y, Miyagawa K, Kanoda K, Maesato M and Saito G 2003 *Phys. Rev. Lett.* **91** 107001
- [204] Yamashita S, Nakazawa Y, Oguni M, Oshima Y, Nojiri H, Shimizu Y, Miyagawa K and Kanoda K 2008 *Nat. Phys.* **4** 459
- [205] Yamashita M, Nakata N, Kasahara Y, Sasaki T, Yoneyama N, Kobayashi N, Fujimoto S, Shibauchi T and Matsuda Y 2009 *Nat. Phys.* **5** 44

- [206] Shimizu Y, Miyagawa K, Kanoda K, Maesato M and Saito G 2006 *Phys. Rev. B* **73** 140407
- [207] Pratt F L, Baker P J, Blundell S J, Lancaster T, Ohira-Kawamura S, Baines C, Shimizu Y, Kanoda K, Watanabe I and Saito G 2011 *Nature* **471** 612
- [208] Poirier M, de Lafontaine M, Miyagawa K, Kanoda K and Shimizu Y 2014 *Phys. Rev. B* **89** 045138
- [209] Itoh K, Itoh H, Saito S, Hosako I, Nakamura Y, Kishida H, Yoneyama N, Sasaki T, Ishihara S and Iwai S 2013 *Phys. Rev. B* **88** 125101